A Recursive-Faulting Model of Distributed Damage in Confined Brittle Materials

A. Pandolfi [a], S. Conti [b], and M. Ortiz [c,*]

[a] *Dipartimento di Ingegneria Strutturale, Politecnico di Milano, Piazza Leonardo da Vinci 32, 20133 Milano, Italy*

[b] *Fachbereich Mathematik, Universität Duisburg-Essen, Lotharstr. 65, 47057 Duisburg, Germany*

[c] *Division of Engineering and Applied Science, California Institute of Technology, Pasadena, CA 91125*

Abstract

We develop a model of distributed damage in brittle materials deforming in triaxial compression based on the explicit construction of special microstructures obtained by *recursive faulting*. The model aims to predict the effective or macroscopic behavior of the material from its elastic and fracture properties; and to predict the microstructures underlying the microscopic behavior. The model accounts for the elasticity of the matrix, fault nucleation and the cohesive and frictional behavior of the faults. We analyze the resulting quasistatic boundary value problem and determine the relaxation of the potential energy, which describes the macroscopic material behavior averaged over all possible fine-scale structures. Finally, we present numerical calculations of the dynamic multi-axial compression experiments on sintered aluminum nitride (AlN) of Chen and Ravichandran [1; 2; 3; 4]. The model correctly predicts the general trends regarding the observed damage patterns; and the brittle-to-ductile transition resulting under increasing confinement confinement.

Key words: Brittle damage, recursive faulting, variational methods, Relaxation, multiscale modelling, multiscale simulation

* Corresponding author

1 Introduction

This paper is concerned with the formulation of a model of distributed damage in brittle materials under triaxial compression. The conditions under consideration here arise in a number of situations of interest, including: geological formations; confined structural ceramics and brittle-matrix composites; crushed concrete; and others. The objectives of the theory are to compute the effective or macroscopic behavior of the material from its elastic and fracture properties; and to predict the microstructures underlying the microscopic behavior. The present work is also concerned with the numerical implementation of the damage model within a concurrent multiscale framework; and with the validation of the model against the experimental data of [2] pertaining to compressive damage in confined ceramics.

Processes of distributed damage in brittle materials have been the subject of extensive research and have been modelled by a variety of means (e. g., [5; 6; 7; 8; 9; 10; 11; 12; 13; 14; 15]). Most of these models are empirical and are based on special solutions from linear elasticity, internal variable formalisms, and other modelling schemes. Local models of distributed damage have also been misapplied to processes of fracture in brittle solids under tension, where fracture mechanics is expected to govern the behavior of the solid. Indeed, the essential distinction between damage and fracture has not always been appreciated fully. Thus, whereas damage is a distributed processes and is described by constitutive laws relating stress to strain, fracture is localized to surfaces and is described, e. g., by cohesive laws relating tractions to opening displacements. One of the aims of the present paper is to elucidate the conditions under which damage occurs in a distributed fashion, and therefore can be described by a damage model. We show that distributed damage occurs when $J = \det(\boldsymbol{F}) < 1$, where $\boldsymbol{F}$ is the average or macroscopic deformation gradient. Thus, distributed damage, as opposed to fracture, is a compressive phenomenon and only occurs when sufficient confinement is present.

The approach followed in the present paper is based on methods of the calculus of variations, especially on recent work on fracture as a free-discontinuity problem [16; 17; 18]. Thus, we suppose that the displacement field jumps discontinuously across a *singular set* of co-dimension 1, and that the energy is composed of two terms: the elastic strain energy obtained by volume integration outside the singular set; and the cohesive fracture energy obtained by surface integration over the singular set (e. g., [19; 18]). However, in contrast to recent work on free-discontinuity problems in fracture mechanics, that has emphasized tensile conditions leading to the formation of isolated dominant cracks, here we envision conditions of triaxial compression resulting in a distributed singular set. We specifically consider singular sets that are composed of *recursive or nested faults*, and show that these microstructures or damage patterns suffice to fully relax the energy.

A recursive fault pattern may be constructed by introducing into the solid a family

of parallel planar cohesive cracks, or *faults*, and subsequently applying that construction recursively to the intervening matrix between the faults. Recursive faulting is similar to the sequential-lamination constructions used to relax non-convex energies arising in other areas of application [20; 21; 22; 23; 24; 25; 26; 27; 28; 29; 30; 31; 32]. In particular, the different levels of faulting are only approximately compatible. However, recursive faulting differs from sequential lamination in some notable respects. Thus, the state of stress within each level of faulting is uniform, and therefore in equilibrium. This greatly simplifies the implementation of recursive faulting relative to sequential lamination algorithms, which must necessarily equilibrate the entire microstructure at considerable computational cost [31; 32]. By contrast, recursive faulting can be implemented simply by means of a recursive call, and the entire microstructure needs not be considered at any time during the construction.

The approximate compatibility between levels of faulting has the effect of building additional misfit elastic energy into the microstructure. We estimate this misfit elastic energy simply by modelling the approximate interfaces as rows of dislocation dipoles. This simple estimate permits the calculation of the separation between the faults, and provides a natural termination criterion for the recursive faulting algorithm. It should be carefully noted that recursive faults are likely to cease being optimal once the misfit elastic energy is taken into consideration. Experience with model problems in martensite and crystal plasticity [33; 34; 35] suggest that more complex microstructures, e. g., involving fault branching, are likely to be optimal instead. However, these enhancements of the theory will not be consider here in the interest of simplicity.

The organization of the paper is as follows. In § 2 the general recursive faulting model is built in steps. We begin by considering rank-1 microstructures consisting of one single level of faulting. The kinematics of such microstructures, the cohesive behavior of the faults and frictional characteristics are formulated in § 2.1, § 2.2, and § 2.6, respectively. In all these and subsequent developments, we strongly rely on variational principles in order to complete the formulation of the model, implement it numerically and analyze it mathematically. In particular, we resort to time discretization in order to coach the incremental problem as a minimum problem. In § 2.4 we exploit this variational structure in order to elucidate conditions for the inception of faulting; and in § 2.5 we resort to the minimum principle and a simple non-local extension of the model in order to determine the optimal separation of the faults. Finally, in § 2.7 we apply rank-1 construction recursively in order to generate more complex microstructures, which we term *recursive faulting* microstructures. The variational formulation also paves the way for an effective mathematical analysis of the quasistatic boundary value problem. The chief analysis tool that we bring to bear on the problem is relaxation. In particular, in § 3 we characterize the relaxation of the recursive-faulting energy functional. This relaxed energy functional describes the macroscopic material behavior averaged over such fine scale structures. In section § 4, as of the range of application of the recur-

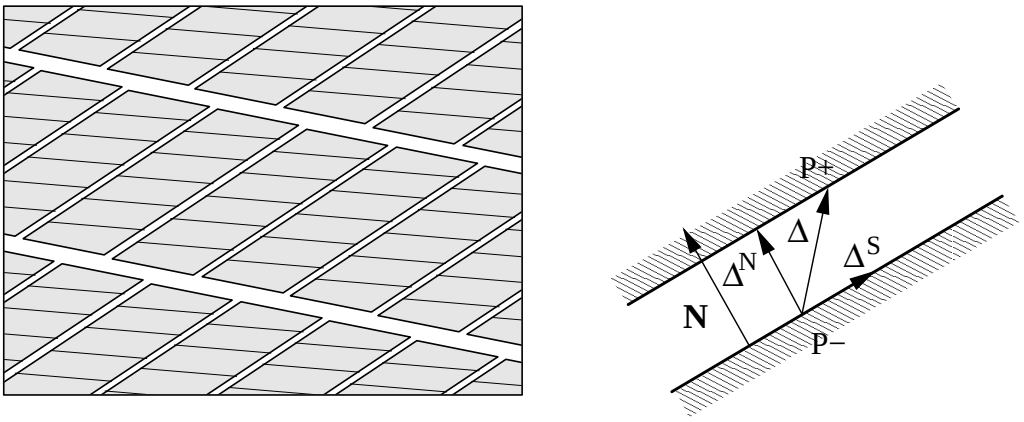

(a) (b)

Fig. 1. (a) Schematic of the assumed kinematics of deformation, showing elastic blocks of matrix material bounded by nested faults. (b) Decomposition of the opening displacement $\boldsymbol{\Delta}$ into normal component and tangential components.

sive faulting model and by way of validation, we proceed to simulate the dynamic multi-axial compression experiments on sintered aluminum nitride (AlN) of Chen and Ravichandran [1; 2; 3; 4]. Finally, concluding remarks and a critical discussion of the model are collected in § 5.

2 Distributed damage by confined recursive faulting

The model is based on a particular class of deformations, or *microstructures*, consisting of nested families of equi-spaced cohesive faults bounding otherwise elastic matrix material. These microstructures are schematically shown in Fig. 1a. We shall refer to this mode of deformation as *recursive faulting*, and the resulting microstructures as *recursive faults*. The primary aim is to devise a means for the effective generation of recursive-fault microstructures and the computation of the effective behavior of the damaged or faulted material. We build the general model in steps. We begin by considering the simple case of one family of faults, and develop the corresponding kinematics of deformation. The assumption of faulting separates the requisite constitutive relations into two independent components: the behavior of the matrix, which we shall assume to be elastic for simplicity; and the behavior of the faults, which we shall assume to be governed by a cohesive relation in the fault initiation stage, and by Coulomb friction and contact henceforth. These aspects of the model are subsequently developed in turn. Finally, we note that the faulting construction can be applied *recursively* in order to generate complex fault patterns.

2.1 Kinematics

We begin by considering the particular case of a single family of fault planes of normal $\boldsymbol{N}$ and spacing L. Assuming strict separation of scales, consider a material vector $d\boldsymbol{X}$ which is short on the scale of the macroscopic deformations but much longer than L. Suppose that $d\boldsymbol{X}$ spans two material points P and Q in the reference configuration. The number of faults traversed by the vector is of the order of

$$n = \frac{1}{L}\, d\boldsymbol{X} \cdot \boldsymbol{N} \tag{1}$$

Suppose that an opening displacement $\boldsymbol{\Delta}$ is applied to each fault, Fig 1b. Let $d\boldsymbol{x}$ be the vector joining P and Q in the deformed configuration. Then,

$$d\boldsymbol{x} = d\boldsymbol{X} + n\boldsymbol{\Delta} = d\boldsymbol{X} + \frac{1}{L}(d\boldsymbol{X} \cdot \boldsymbol{N})\boldsymbol{\Delta} = (\boldsymbol{I} + \frac{1}{L}\boldsymbol{\Delta} \otimes \boldsymbol{N})d\boldsymbol{X} \equiv \boldsymbol{F}^p d\boldsymbol{X} \tag{2}$$

where

$$\boldsymbol{F}^p = \boldsymbol{I} + \frac{1}{L}\boldsymbol{\Delta} \otimes \boldsymbol{N} \tag{3}$$

may be regarded as the discontinuous or singular deformation component due to fault activity. Suppose in addition that the matrix is given a uniform deformation $\boldsymbol{F}^e$. Then

$$d\boldsymbol{x} = \boldsymbol{F} d\boldsymbol{X} \tag{4}$$

where

$$\boldsymbol{F} = \boldsymbol{F}^e \boldsymbol{F}^p \tag{5}$$

Thus we arrive at a multiplicative decomposition of the deformation gradient into a discontinuous and a matrix component. We note that, once $\boldsymbol{N}$ and L are supplied, $\boldsymbol{F}^p$ and $\boldsymbol{\Delta}$ are in one-to-one correspondence. In particular, the opening displacements $\boldsymbol{\Delta}$ follow from $\boldsymbol{F}^p$ through the relation

$$\boldsymbol{\Delta} = L\,(\boldsymbol{F}^p - \boldsymbol{I}) \cdot \boldsymbol{N} \tag{6}$$

We also note that the inverse of the $\boldsymbol{F}^p$ follows simply by an application of the Sherman-Morrison formula to (3), with the result:

$$\boldsymbol{F}^{p-1} = \boldsymbol{I} - \frac{1}{L + \boldsymbol{\Delta} \cdot \boldsymbol{N}}\boldsymbol{\Delta} \otimes \boldsymbol{N} \tag{7}$$

2.2 Cohesive stage

We assume that during the early states of damage immediately following the inception of of the faults, or *cohesive stage*, the opening of the faults is resisted by cohesive forces. In addition, we confine our attention to brittle materials that behave

elastically in the absence of damage. A form of the free energy density consistent with these assumptions is:

$$A(\boldsymbol{F},\theta,\boldsymbol{\Delta},\boldsymbol{q}) = W^e(\boldsymbol{F}^e,\theta) + \frac{1}{L}\Phi(\theta,\boldsymbol{\Delta},\boldsymbol{q}) \tag{8}$$

where W is the elastic strain-energy density per unit volume of the matrix, Φ is the cohesive energy per unit fault surface, θ is the absolute temperature, and $\boldsymbol{q}$ is some appropriate set of internal variables describing the state of the faults. The additive structure (8) of the free energy density is in line with general mathematical results pertaining to free-discontinuity problems. By material-frame indifference, it follows that W^e can only depend on $\boldsymbol{F}^e$ through the matrix right Cauchy-Green deformation tensor:

$$\boldsymbol{C}^e = \boldsymbol{F}^{eT}\,\boldsymbol{F}^e = \boldsymbol{F}^{p-T}\,\boldsymbol{C}\,\boldsymbol{F}^{p-1} \tag{9}$$

where $\boldsymbol{C} = \boldsymbol{F}^T\boldsymbol{F}$ is the right Cauchy-Green deformation tensor, whereupon (8) simplifies to:

$$A(\boldsymbol{F},\theta,\boldsymbol{\Delta},\boldsymbol{q}) = W^e(\boldsymbol{C}^e,\theta) + \frac{1}{L}\Phi(\theta,\boldsymbol{\Delta},\boldsymbol{q}) \tag{10}$$

A simple class of three-dimensional cohesive laws governing the cohesive stage of the faults can be constructed as follows. Following [36], we begin by introducing an effective opening displacement of the form, Fig. 1b:

$$\Delta = \sqrt{(1-\beta^2)(\boldsymbol{\Delta}\cdot\boldsymbol{N})^2 + \beta^2|\boldsymbol{\Delta}|^2} \tag{11}$$

where $|\boldsymbol{\Delta}|$ is the magnitude or norm of $\boldsymbol{\Delta}$ and β is a material constant which assigns different weights to the normal and tangential components of the opening displacement. We now assume that the cohesive energy $\Phi(\theta,\boldsymbol{\Delta},\boldsymbol{q})$ depends on $\boldsymbol{\Delta}$ only through the effective opening displacement Δ. In addition, we restrict attention to isothermal processes and omit all explicit references to the temperature θ for simplicity of notation. Under these conditions the cohesive potential takes the form

$$\Phi = \Phi(\Delta,\boldsymbol{q}) \tag{12}$$

The corresponding cohesive tractions are:

$$\boldsymbol{T} = \frac{\partial\Phi}{\partial\boldsymbol{\Delta}} = \frac{T}{\Delta}[(1-\beta^2)(\boldsymbol{\Delta}\cdot\boldsymbol{N})\boldsymbol{N} + \beta^2\boldsymbol{\Delta}] \equiv T\boldsymbol{d} \tag{13}$$

and the configurational force conjugate to $\boldsymbol{N}$, or configurational torque, is

$$\frac{\partial\Phi}{\partial\boldsymbol{N}} = \frac{T}{\Delta}(1-\beta^2)(\boldsymbol{\Delta}\cdot\boldsymbol{N})\boldsymbol{\Delta} \tag{14}$$

where

$$T = \frac{\partial\Phi}{\partial\Delta}(\Delta,\boldsymbol{q}) \tag{15}$$

is the effective traction and $\boldsymbol{d}$ is the traction direction. The tangent stiffness of the cohesive plane is given by:

$$\boldsymbol{K} = \frac{\partial^2 \Phi}{\partial \boldsymbol{\Delta} \partial \boldsymbol{\Delta}} = \left(K - \frac{T}{\Delta} \right) \boldsymbol{d} \otimes \boldsymbol{d} + \frac{T}{\Delta} [(1 - \beta^2) \boldsymbol{N} \otimes \boldsymbol{N} + \beta^2 \boldsymbol{I}] \tag{16}$$

where

$$K = \frac{\partial T}{\partial \Delta}(\Delta, \boldsymbol{q}) \tag{17}$$

is the effective stiffness of the cohesive plane. A simple calculation gives the identity

$$T = \sqrt{(1 - \beta^{-2})(\boldsymbol{T} \cdot \boldsymbol{N})^2 + \beta^{-2} |\boldsymbol{T}|^2} \tag{18}$$

which shows that T is a weighted combination of the normal and tangential tractions to the fault.

Following [37; 36], we render the cohesive law irreversible by assuming unloading to the origin. In this model, the sole internal variable q of the material is the maximum attained effective opening displacement, and the corresponding kinetic equation is, therefore,

$$\dot{q} = \begin{cases} \dot{\Delta}, & \text{if } \Delta = q \text{ and } \dot{\Delta} \geq 0 \\ 0, & \text{otherwise} \end{cases} \tag{19}$$

The first of these cases corresponds to *loading* or the faults and the second case to *unloading*. Let $\Phi_0(\Delta)$ be the monotonic cohesive energy, i. e., a function such that

$$T_0(\Delta) = \frac{\partial \Phi_0}{\partial \Delta}(\Delta) \tag{20}$$

$$K_0(\Delta) = \frac{\partial T_0}{\partial \Delta}(\Delta) \tag{21}$$

are the effective tractions and stiffness under monotonically growing Δ. Then, the cohesive energy and its derivatives follows as

$$\Phi(\Delta, q) = \Phi_0(q) + \frac{1}{2} \frac{T_0(q)}{q} (\Delta^2 - q^2) \tag{22}$$

$$T(\Delta, q) \equiv \frac{\partial \Phi}{\partial \Delta}(\Delta, q) = \frac{T_0(q)}{q} \Delta \tag{23}$$

$$-Y(\Delta, q) \equiv \frac{\partial \Phi}{\partial q}(\Delta, q) = \frac{1}{2} \Big[K_0(q) q - T_0(q) \Big] \Big[(\Delta / q)^2 - 1 \Big] \tag{24}$$

$$K(\Delta, q) \equiv \frac{\partial T}{\partial \Delta}(\Delta, q) = \begin{cases} K_0(q), & \text{loading} \\ T_0(q)/q, & \text{unloading} \end{cases} \tag{25}$$

where $Y(\Delta, q)$ is the thermodynamic driving force for damage. We shall assume throughout the inequality

$$K_0(q) q < T_0(q), \tag{26}$$

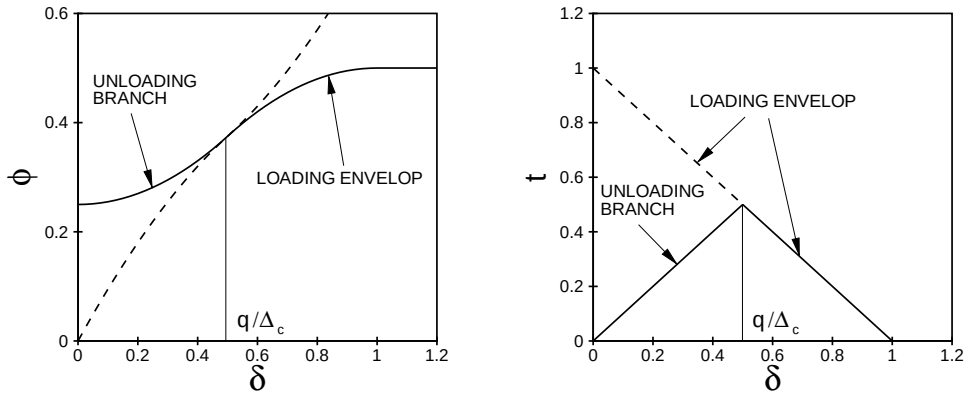

(a) (b)

Fig. 2. Linearly decreasing cohesive envelop.

which ensures that unloading to the origin is well defined. This inequality is satisfied by all commonly used cohesive envelops.

For lack of a better term, we shall refer to the cohesive model described in the foregoing, consisting in the introduction of a scalar effective opening displacement, a monotonic cohesive envelop and unloading to the origin, as the *effective opening displacement* (EOD) cohesive model. In calculations we additionally use the simple cohesive envelop [37; 38; 39]:

$$\Phi_0 = \begin{cases} T_c\Delta - T_c\Delta^2/2\Delta_c, & \text{if } \Delta \leq \Delta_c \\ G_c = T_c\Delta_c/2, & \text{otherwise} \end{cases} \tag{27}$$

The corresponding cohesive law consists of rigid behavior, i. e., $\Delta = 0$, for $T < T_c$, followed by a linearly decreasing dependence of T on Δ for $\Delta < \Delta_c$, and $T = 0$ thenceforth, Fig. 2.

2.3 Time discretization

We shall strongly rely on variational principles in order to complete the formulation of the model, implement it numerically and analyze it mathematically. The behavior of irreversible materials can be characterized variationally by recourse to time discretization. To this end, we envision a process of incremental deformation and seek to determine the state of the material at times $t_0, \ldots, t_{n+1} = t_n + \Delta t, \ldots$. Suppose that the state of the material is known at time t_n and let the deformation $\boldsymbol{F}_{n+1}$ at time t_{n+1} be given. The problem is to determine the state of the material at time t_{n+1}.

We begin by considering the case in which one family of faults is present in the material and the behavior of the faults is cohesive. Following [40] we define an

incremental strain-energy density

$$W_n(\boldsymbol{F}_{n+1}) = \inf_{\substack{\boldsymbol{\Delta}_{n+1},\, q_{n+1} \\ \boldsymbol{\Delta}_{n+1}\cdot\boldsymbol{N}\geq 0 \\ q_{n+1}\geq q_n}} A(\boldsymbol{F}_{n+1}, \boldsymbol{\Delta}_{n+1}, q_{n+1}) \tag{28}$$

We note that by virtue of the irreversibility constraint, $q_{n+1} \geq q_n$, $W_n(\boldsymbol{F}_{n+1})$ depends tacitly on the initial conditions at time t_n. We signify this dependence by means of the subindex n. In particular, $W_n(\boldsymbol{F}_{n+1})$ varies between time steps, which allows for irreversibility, hysteresis and path dependency. It can be shown [40] that $W_n(\boldsymbol{F}_{n+1})$ acts as a potential for the first Piola-Kirchhoff stress tensor $\boldsymbol{P}_{n+1}$ at time t_{n+1}, i. e., as

$$\boldsymbol{P}_{n+1} = \frac{\partial W_n}{\partial \boldsymbol{F}_{n+1}}(\boldsymbol{F}_{n+1}) \tag{29}$$

Consequently, the stable equilibrium configurations can be characterized as the minimizers of the corresponding potential energy.

The constraints appended to the minimum problem (28) can be enforced by means of Lagrange multipliers. The corresponding optimality conditions are (cf, e. g., [41])

$$\frac{\partial}{\partial \Delta_I}[A + \lambda_1 \boldsymbol{\Delta}\cdot\boldsymbol{N}] = -\frac{1}{L + \boldsymbol{\Delta}\cdot\boldsymbol{N}} N_J \frac{\partial W}{\partial F^e_{iJ}} F^e_{iI} + \frac{1}{L}\frac{\partial \Phi}{\partial \Delta_I} + \lambda_1 N_I = 0 \tag{30a}$$

$$\frac{\partial}{\partial q}[A + \lambda_2 (q - q_n)] = \frac{1}{L}\frac{\partial \Phi}{\partial q} + \lambda_2 = 0 \tag{30b}$$

$$\boldsymbol{\Delta}\cdot\boldsymbol{N} \geq 0, \quad \lambda_1 \leq 0 \quad \text{and} \quad \lambda_1 \boldsymbol{\Delta}\cdot\boldsymbol{N} = 0 \tag{30c}$$

$$q - q_n \geq 0, \quad \lambda_2 \leq 0 \quad \text{and} \quad \lambda_2 (q - q_n) = 0 \tag{30d}$$

where here and subsequently we have omitted the subindex $n + 1$ for clarity of notation. For the EOD cohesive model, the tractions $\partial_{\boldsymbol{\Delta}}\Phi$ in (30a) are given by (13), (15) and (23); and the driving force $-\partial_q \Phi$ in (30b) is given by (24). It is clear from the optimality conditions that λ_1 may be regarded as a contact normal traction and λ_2 as a driving force for damage. The Kuhn-Tucker condition (30c) then requires that the contact tractions be compressive during contact or zero during opening; and the Kuhn-Tucker condition (30d) then requires that the driving for damage be zero during damage or negative during unloading. These latter conditions are in analogy to rate-independent models of plasticity, which require the material to be at yield, i. e., the overstress to be zero during plastic deformation; and the response to be elastic when the material is below yield, i. e., when the overstress is negative.

A strategy for finding optimal solutions consists in looking first for an unloaded open-fault solution, i. e., assuming $\boldsymbol{\Delta}\cdot\boldsymbol{N} \geq 0$ and $q = q_n$. In this case, $\lambda_1 = 0$, $\lambda_2 \geq 0$. Therefore, $\boldsymbol{\Delta}$ can be computed directly from (30a), e. g., by a Newton-

Raphson iteration. The requisite tangents for this iteration are

$$L\frac{\partial^2 A}{\partial\Delta_I\partial\Delta_K} = \frac{\partial^2\Phi}{\partial\Delta_I\partial\Delta_K} + \frac{L}{(L+\boldsymbol{\Delta}\cdot\boldsymbol{N})^2} \left[\frac{\partial^2 W}{\partial F^e_{iJ}\partial F^e_{kL}}F^e_{iI}F^e_{kK}N_L + \frac{\partial W}{\partial F^e_{iJ}}F^e_{iK}N_I + \frac{\partial W}{\partial F^e_{iJ}}F^e_{iI}N_K\right] N_J \tag{31}$$

In addition, it follows from (30b) and (24) that $\Delta \leq q_n$. In reaching this conclusion we have used the constitutive inequality (26). Thus, the solution is valid if $\boldsymbol{\Delta}$ satisfies the inequalities: $\boldsymbol{\Delta}\cdot\boldsymbol{N} \geq 0$ and $\Delta \leq q_n$. Suppose now that the unloading-opening predictor fails to return a feasible solution. Then we repeat the calculation by activating the most violated constraint, i. e., we activate the contact constraint if $|\boldsymbol{\Delta}\cdot\boldsymbol{N}| < |q - q_n|$, and we activate damage if $|q - q_n| < |\boldsymbol{\Delta}\cdot\boldsymbol{N}|$. The iteration terminates when all the optimality conditions are satisfied simultaneously.

Once the optimal values of $\boldsymbol{\Delta}$ and q at time t_{n+1} are know, the first Piola-Kirchhoff stress tensor follows from (29) as

$$P_{Ji} = \frac{\partial W_n}{\partial F_{iJ}} = \left(\frac{\partial W}{\partial F^e_{iK}}F^e_{kK}\right)F^{-1}_{Jk} \tag{32}$$

The term is parenthesis follows directly from the elasticity of the matrix. The consistent tangent moduli follow by linearization of (29), i. e.,

$$D\boldsymbol{P}_{n+1} = \frac{\partial^2 W_n}{\partial\boldsymbol{F}_{n+1}\partial\boldsymbol{F}_{n+1}}(\boldsymbol{F}_{n+1}) \tag{33}$$

Evidently, the tangent moduli are symmetric owing to the potential character of the incremental stress-strain relations. A straightforward calculation gives

$$\frac{\partial P_{Ji}}{\partial F_{kL}} = \frac{\partial^2 W_n}{\partial F_{iJ}\partial F_{kL}} = \frac{\partial^2 A}{\partial F_{iJ}\partial F_{kL}} - \frac{\partial^2 A}{\partial F_{iJ}\partial\Delta_M}\left(\frac{\partial^2 A}{\partial\Delta_M\partial\Delta_N}\right)^{-1}\frac{\partial^2 A}{\partial\Delta_N\partial F_{kL}} \tag{34}$$

Again, the first term in this expression follows directly from the elasticity of the matrix as

$$\frac{\partial^2 A}{\partial F_{iJ}\partial F_{kL}} = \frac{\partial^2 W}{\partial F^e_{iM}\partial F^e_{kN}}(F^p)^{-1}_{JM}(F^p)^{-1}_{LN} \tag{35}$$

The second derivatives of A with respect to $\boldsymbol{\Delta}_{n+1}$ are given in (16). Finally, the cross derivatives required to evaluate the tangents (34) are found to be:

$$\frac{\partial^2 A}{\partial F_{iJ}\,\partial\Delta_K} = -\frac{1}{L+\boldsymbol{\Delta}\cdot\boldsymbol{N}}\left(\frac{\partial^2 W}{\partial F^e_{iL}\partial F^e_{nM}}F^e_{nK}F^e_{mL} + \frac{\partial W}{\partial F^e_{iM}}F^e_{mK}\right)F^{-1}_{Jm}N_M \tag{36}$$

2.4 Fault inception and orientation

Suppose that the material is undamaged at time t_n and that we are given the deformation $\boldsymbol{F}_{n+1}$ at time t_{n+1}. We wish to determine whether in insertion of faults is energetically favorable; and the optimal orientation of the faults. We ascertain these questions with the aid of the time-discretized variational formulation developed in the preceding question. Thus, for the given deformation $\boldsymbol{F}_{n+1}$ we test two end states of the material, one with faults and another without faults. The orientation of the faults in the latter state is obtained variationally, as described in this section. We then choose the end state which results in the lowest incremental energy density $W_n(\boldsymbol{F}_{n+1})$.

The optimal orientation $\boldsymbol{N}$ of the faults and the remaining state variables at time t_{n+1} follow from the extended minimum problem:

$$
\begin{aligned}
W_n(\boldsymbol{F}_{n+1}) = \quad & \inf_{\substack{\boldsymbol{\Delta}_{n+1},\, q_{n+1},\, \boldsymbol{N} \\ \boldsymbol{\Delta}_{n+1}\cdot\boldsymbol{N}\geq 0 \\ q_{n+1}\geq q_n \\ |\boldsymbol{N}|^2=1}} A(\boldsymbol{F}_{n+1}, \boldsymbol{\Delta}_{n+1}, q_{n+1}, \boldsymbol{N})
\end{aligned}
\tag{37}
$$

The corresponding optimality conditions are

$$
\frac{\partial}{\partial \Delta_I}[A + \lambda_1 \boldsymbol{\Delta}\cdot\boldsymbol{N}] = -\frac{1}{L+\boldsymbol{\Delta}\cdot\boldsymbol{N}} N_J \frac{\partial W^e}{\partial F^e_{iJ}} F^e_{iI} + \frac{1}{L}\frac{\partial \Phi}{\partial \Delta_I} + \lambda_1 N_I = 0 \tag{38a}
$$

$$
\frac{\partial}{\partial q}[A + \lambda_2 (q - q_n)] = \frac{1}{L}\frac{\partial \Phi}{\partial q} + \lambda_2 = 0 \tag{38b}
$$

$$
\begin{aligned}
&\frac{\partial}{\partial N_I}[A + \lambda_1 \boldsymbol{\Delta}\cdot\boldsymbol{N} + \lambda_3 |\boldsymbol{N}|^2] = \\
&\qquad - \frac{\Delta_J}{L+\boldsymbol{\Delta}\cdot\boldsymbol{N}} \frac{\partial W^e}{\partial F^e_{iJ}} F^e_{iI} + \frac{1}{L}\frac{\partial \Phi}{\partial N_I} + \lambda_1 \Delta_I + 2\lambda_3 N_I = 0
\end{aligned}
\tag{38c}
$$

$$
\boldsymbol{\Delta}\cdot\boldsymbol{N} \geq 0, \quad \lambda_1 \leq 0 \quad \text{and} \quad \lambda_1 \boldsymbol{\Delta}\cdot\boldsymbol{N} = 0 \tag{38d}
$$

$$
q - q_n \geq 0, \quad \lambda_2 \leq 0 \quad \text{and} \quad \lambda_2 (q - q_n) = 0 \tag{38e}
$$

$$
|\boldsymbol{N}|^2 = 1 \tag{38f}
$$

For the EOD cohesive model the configurational torque $-\partial_{\boldsymbol{N}}\Phi$ in (38c) is given by (14), (15) and (23).

Suppose that the incipient fault undergoes opening, i. e., $\boldsymbol{\Delta}\cdot\boldsymbol{N} > 0$ and, correspondingly, $\lambda_1 = 0$. Then, it is possible to satisfy eqs. (38a) and (38c) simultaneously by setting $\boldsymbol{\Delta} = (\boldsymbol{\Delta}\cdot\boldsymbol{N})\boldsymbol{N}$. This identity in turn implies that the normal to the incipient fault aligns itself with the direction of opening. Then (38a) and (38c)

reduce to the symmetric eigenvalue problem

$$S^e_{IJ}N_J = \Lambda N_I \tag{39}$$

where

$$S^e_{IJ} = F^e_{iI}\frac{\partial W^e}{\partial F^e_{iJ}} \tag{40}$$

is a symmetric second Piola-Kirchhoff stress tensor for the matrix, and

$$\Lambda = (L + \boldsymbol{\Delta}\cdot\boldsymbol{N})\frac{T}{L} = (L + \boldsymbol{\Delta}\cdot\boldsymbol{N})\left(\frac{T}{L}(1-\beta^2) + \frac{2\lambda_3}{\boldsymbol{\Delta}\cdot\boldsymbol{N}}\right) \tag{41}$$

It follows from the first of these identities that the eigenvalue Λ is a tensile principal stress of the matrix and, therefore, the case under consideration fails to yield solutions if the stress in the matrix is compressive in all directions. In cases of multiaxial tension, the largest tensile direction is energetically favorable since, by eq. (41), it corresponds to the largest effective traction T and hence results in the least expense of cohesive energy. When two or three of the principal stresses of the matrix are tensile and equal the optimal value of $\boldsymbol{N}$ is indeterminate and, in calculations, is chosen randomly.

Suppose that the matrix is in all around compression. Then the incipient faults are necessarily closed and deform by sliding, i. e., $\boldsymbol{\Delta}\cdot\boldsymbol{N} = 0$. Under these conditions, inserting (13) and (14) into (38a) and (38c) gives

$$-\frac{1}{L}S^e_{IJ}N_J + \frac{\beta T}{L}M_I + \lambda_1 N_I = 0 \tag{42}$$

$$-\frac{1}{L}S^e_{IJ}M_J + \lambda_1 M_I + \frac{2\lambda_3}{|\boldsymbol{\Delta}|}N_I = 0 \tag{43}$$

where $\boldsymbol{M} = \boldsymbol{\Delta}/|\boldsymbol{\Delta}|$ is the unit vector in the direction of $\boldsymbol{\Delta}$. Multiplying the first of these equations by $\boldsymbol{M}$ and the second by $\boldsymbol{N}$ we obtain the identities

$$\frac{1}{L}S^e_{IJ}M_I N_J = \frac{\beta T}{L} = \frac{2\lambda_3}{|\boldsymbol{\Delta}|} \tag{44}$$

The resulting equations imply that $\boldsymbol{N}$ is a plane of maximum shear of the matrix stress $\boldsymbol{S}^e$.

In summary, faults can form in two modes: opening and sliding. In the opening mode, the faults orient themselves so that their normal is aligned with the direction of opening. This mode can only occur if at least one of the principal directions of stress in the matrix is tensile. In the sliding mode, the incipient faults orient themselves along planes of maximum shear of the matrix. The sliding mode can operate when there are maximum shear planes that are under normal compression. In cases in which both the opening and sliding modes can operate, they are evaluated in turn and the operative mode is chosen to be the energy-minimizing one.

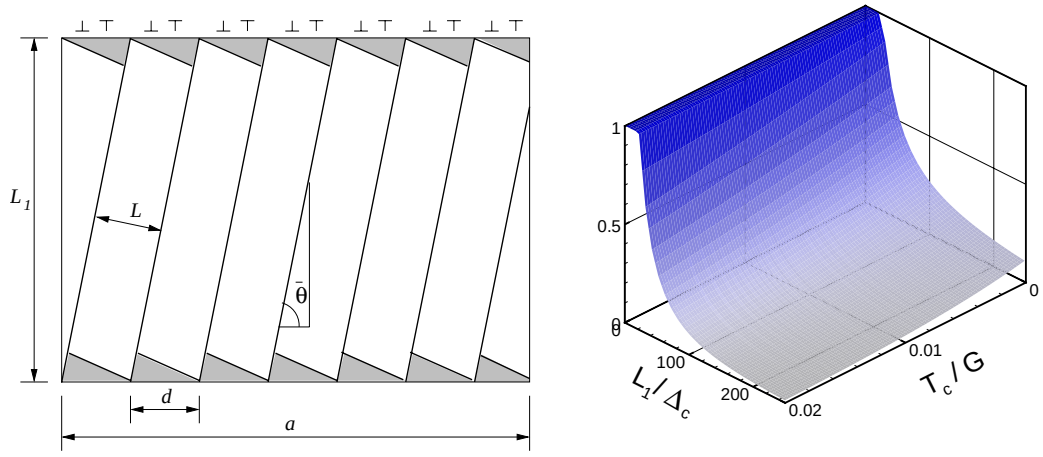

(a) (b)

Fig. 3. a) Dislocation model used to estimate the misfit energy. b) Plot of the optimum L as function of T_c/G and L_1/Δ_c for the piecewise-linear cohesive law. In the plot we take L_0 = 10 Δ_c.

2.5 Nonlocal extension and the size of the microstructure

In the previous developments, the length L has been regarded as a known parameter. Alternatively, it can be computed variationally as part of the incremental update (28). However, in order to obtain meaningful values of the fault spacing L it is important to account for the *misfit energy*, i. e., the energy contained in the boundary layers that forms where the faults meet a confining boundary, Fig. 3a. Thus, the compatibility between the faults and their container is only *approximate*, or on average, and this gives rise to boundary layers that penetrate into the faulted region to a certain depth.

In order to estimate the misfit energy, and subsequently compute the resulting optimal spacing between faults, we model the boundary layer as an array of dislocations of alternating sign, Fig. 3. The Burgers vector of the misfit dislocations is of the order of $|\boldsymbol{\Delta}|$. This suggests the model misfit energy density

$$E^{\text{mis}}(\boldsymbol{\Delta}, L) = C\frac{|\boldsymbol{\Delta}|^2}{L_1}\frac{1}{L}\log\frac{L}{L_0} \tag{45}$$

where C is a constant elastic modulus, L_1 the size of the confining container and L_0 plays the role of a 'core cut off'. Accounting for the misfit energy, the total free-energy density of the faulted region becomes

$$\begin{aligned} &A(\boldsymbol{F}_{n+1}, \boldsymbol{\Delta}_{n+1}, q_{n+1}, L_{n+1}) = \\ &W^e(\boldsymbol{F}^e_{n+1}, L_{n+1}) + \frac{1}{L_{n+1}}\Phi(\boldsymbol{\Delta}_{n+1}, \boldsymbol{q}_{n+1}) + E^{\text{mis}}(\boldsymbol{\Delta}_{n+1}, L_{n+1}) \end{aligned} \tag{46}$$

The variational update (28) now becomes

$$W_n(\boldsymbol{F}_{n+1}) = \inf_{\substack{\boldsymbol{\Delta}_{n+1},\, q_{n+1},\, L_{n+1} \\ \boldsymbol{\Delta}_{n+1}\cdot\boldsymbol{N}\geq 0 \\ q_{n+1}\geq q_n}} A(\boldsymbol{F}_{n+1}, \boldsymbol{\Delta}_{n+1}, q_{n+1}, L_{n+1}) \tag{47}$$

It is clear from the form of the free energy (46) and, in particular, of the misfit energy (45) that the optimal fault separation is determined by two competing demands. On one hand, the cohesive energy favors a large value of L resulting in fewer faults per unit volume. On the other hand, the misfit energy favors a small value of L resulting in a narrow boundary layer. Minimization with respect to L_{n+1} gives the equation

$$\frac{1}{L^2}\left(\frac{\partial\Phi}{\partial\Delta_K}\Delta_K - \Phi + \frac{C|\boldsymbol{\Delta}|^2}{L_1} - \frac{C|\boldsymbol{\Delta}|^2}{L_1}\log\frac{L}{L_0}\right) = 0 \tag{48}$$

whence we find

$$L = L_0 \exp\left[1 - \frac{L_1}{C}\Gamma(\boldsymbol{\Delta})\right] \tag{49}$$

where

$$\Gamma(\boldsymbol{\Delta}) = \frac{1}{|\boldsymbol{\Delta}|^2}\left[\Phi(\boldsymbol{\Delta}) - \frac{\partial\Phi}{\partial\Delta_K}\Delta_K\right] \tag{50}$$

For the EOD model with a linearly decreasing monotonic envelop we obtain the particularly simple result

$$\Gamma(\boldsymbol{\Delta}) = \frac{T_c}{2\Delta_c} = \text{constant} \tag{51}$$

and the corresponding fault separation follows explicitly as

$$L = L_0 \exp\left[1 - \frac{L_1}{C}\frac{T_c}{2\Delta_c}\right] \tag{52}$$

independently of the opening displacement $\boldsymbol{\Delta}$. Thus, in this model the separation between the faults is set at the inception of the faults and conveniently remains constant thereafter. The resulting dependence of L/L_1 on the parameters T_c/G and L_1/Δ_c is shown in Fig. 3b, where G is the shear modulus, and we take L_0 = 10 Δ_c. As expected, L decreases with increasing cohesive strength T_c and critical opening displacement Δ_c, since an increase in these parameters implies a corresponding increase in the specific cohesive energy of the material.

2.6 Frictional stage

Internal *friction* is an important dissipation mechanism in brittle materials, especially in geological applications, applications to structural ceramics, and others. We shall therefore assume that friction operates at the faults *concurrently* with cohesion. However, if the faults loose cohesion completely, e. g., upon the attainment of a critical opening displacement, friction may become the sole dissipation mechanism at the faults.

In considering friction, we wish to retain the variational structure of the model. In particular, we wish to define an incremental strain energy density $W_n(\boldsymbol{F}_{n+1})$ with the property that it be a potential for the stresses through relation (29). To this end, we follow Pandolfi *et al.* [42] and define the extended update

$$
\begin{aligned}
&W_n(\boldsymbol{F}_{n+1}) = \\
&\qquad \inf_{\boldsymbol{\Delta}_{n+1},\, q_{n+1}} \quad A(\boldsymbol{F}_{n+1}, \boldsymbol{\Delta}_{n+1}, q_{n+1}) + \frac{\Delta t}{L}\, \psi^*\left(\frac{\boldsymbol{\Delta}_{n+1} - \boldsymbol{\Delta}_n}{\Delta t}; \boldsymbol{F}_{n+1}, \boldsymbol{\Delta}_{n+1}, q_{n+1}\right) \\
&\boldsymbol{\Delta}_{n+1} \cdot \boldsymbol{N} \geq 0 \\
&\qquad q_{n+1} \geq q_n
\end{aligned}
\tag{53}
$$

where for simplicity we consider the case of $L =$ constant. In (53) $\psi^*(\dot{\boldsymbol{\Delta}}; \boldsymbol{F}, \boldsymbol{\Delta}, q)$ is a dual kinetic potential per unit area with the following properties:

i) $\psi^* = 0$ if the contact traction $\lambda_1 = 0$, cf eq. (30c), i. e., if the faults undergo opening.
ii) If $\lambda_1 < 0$, cf eq. (30c), i. e., if the faults are closed, then $\psi^*(\,\cdot\,; \boldsymbol{F}, \boldsymbol{\Delta}, q)$ is convex and is minimized at $\dot{\boldsymbol{\Delta}} = \boldsymbol{0}$.

We note that during closure, $\lambda_1 < 0$, the contact constraint $\boldsymbol{\Delta} \cdot \boldsymbol{N} = 0$ is active and only the *sliding* opening displacements are nonzero. Hence, frictional dissipation is always associated with fault sliding, as required. We also note that, upon multiplication by $\boldsymbol{N}$, the equilibrium equation (30a) gives the contact traction in the form

$$
\lambda_1 = \frac{1}{L}\left(\boldsymbol{N} \cdot S^e \boldsymbol{N} - \frac{\partial \Phi}{\partial \boldsymbol{\Delta}} \cdot \boldsymbol{N}\right) \tag{54}
$$

Thus, condition (i) can be restated as the requirement that $\psi^* = 0$ if the right hand side of (54) vanishes. In the presence of friction, the traction equilibrium equation (30a) becomes

$$
\frac{1}{L}\left[-S^e_{IJ} N_J + \frac{\partial \Phi}{\partial \Delta_I} + \partial_{\dot{\boldsymbol{\Delta}}} \psi^*\left(\frac{\boldsymbol{\Delta} - \boldsymbol{\Delta}_n}{\Delta t}; \boldsymbol{F}, \boldsymbol{\Delta}, q\right)\right] + \lambda_1 N_I = O(\Delta t) \tag{55}
$$

where the terms of order $O(\Delta t)$ arise from the dependence of ψ^* on the state variables $(\boldsymbol{F}, \boldsymbol{\Delta}, q)$. As expected, the frictional forces contribute to the equilibrium of tangential tractions at the faults. It is evident from (55) that the update (53) is consistent with the frictional rate equations up to admissible truncation errors of order $O(\Delta t)$.

In calculations we assume Coulomb friction and set

$$\psi^*(\dot{\boldsymbol{\Delta}}; \boldsymbol{F}, \boldsymbol{\Delta}, q) = \mu \max\left\{0,\ \frac{\partial \Phi}{\partial \boldsymbol{\Delta}} \cdot \boldsymbol{N} - \boldsymbol{N} \cdot S^e \boldsymbol{N}\right\} |\dot{\boldsymbol{\Delta}}| \tag{56}$$

where μ is the coefficient of friction. We note that this choice of dual dissipation potential satisfies conditions (i) and (ii), as required. As befits Coulomb friction, the kinetic potential (56) is rate-independent, i. e., is positively homogeneous of degree 1 in $\dot{\boldsymbol{\Delta}}$, and proportional to the contact pressure. We also note that for the EOD model $\partial_{\boldsymbol{\Delta}} \Phi \cdot \boldsymbol{N} = 0$ if $\boldsymbol{\Delta} \cdot \boldsymbol{N} = 0$ and (56) simplifies to

$$\psi^*(\dot{\boldsymbol{\Delta}}; \boldsymbol{F}, \boldsymbol{\Delta}, q) = \mu \max\left\{0,\ -\boldsymbol{N} \cdot S^e \boldsymbol{N}\right\} |\dot{\boldsymbol{\Delta}}| \tag{57}$$

It should be carefully noted that the variational formulation (53) of fault friction, and the more general one of Pandolfi *et al.* [42], is non-standard in that it results in an incremental minimization problem. In particular, the tangent stiffness corresponding to the incremental equilibrium problem is symmetric, contrary to what is generally expected of *non-associative* materials. The difference between a direct, or non-symmetric, and a variational update for these materials resides in the $O(\Delta t)$ terms in eq. (55). Thus, these terms ensure the variational structure of the update without affecting its consistency. In particular, as already mentioned, the variational update defines an incremental strain-energy density $W_n(\boldsymbol{F}_{n+1})$ with the fundamental property (29), as desired.

2.7 Recursive faulting

So far we have consider either an intact material or a single family of parallel faults. We shall refer to the latter microstructure as a *rank*-1 faulting pattern. More complex microstructures, which we name *recursive faulting patterns*, can effectively be generated by applying the rank-1 construction *recursively*. In the first level of recursion, in (8) and (28) we simply replace the elastic strain-energy density $W(\boldsymbol{F}^e)$ of the matrix by $W_n(\boldsymbol{F}^e)$, i. e., by the effective strain-energy density of a rank-1 faulting pattern. This substitution can now be iterated, resulting in a recursive definition of $W_n(\boldsymbol{F}_{n+1})$. The recursion stops when $W_n(\boldsymbol{F}^e) = W(\boldsymbol{F}^e)$, i. e., when intervening matrix between the faults remains elastic. The resulting microstructures are shown in Fig. 1a, and consist of *faults within faults*. The level of recursion is the *rank* of the microstructure.

As noted in the introduction, recursive faulting is similar in spirit to the sequential-lamination constructions used to relax non-convex energies arising in other areas of application (cf, e. g., [21; 26] and references therein). In particular, as in laminates the different levels of faulting are only approximately compatible. However, recursive faulting differs from sequential lamination crucially in that the state of stress within each level of faulting is uniform, and therefore automatically in equilibrium. The implication of this property is that the recursive faulting construction can be implemented simply by means of a recursive call to the rank-1 faulting construction. Conveniently, many programming languages such as C or C++ support recursive function calls. This greatly facilitates the implementation of the model, which is reduced to the implementation of the rank-1 faulting construction. This is in sharp contrast to laminates, which must be equilibrated globally at considerable computational cost and complexity of implementation (cf [31; 32]).

3 Relaxation of the recursive faulting model

Next we turn to the boundary value problem of a solid undergoing recursive faulting such as described in the foregoing and proceed to analyze its properties. In order to simplify the analysis we work within a *deformation theory* framework, namely, we consider the incremental strain-energy density $W(\boldsymbol{F})$ that results from applying the entire deformation $\boldsymbol{F}$ to an intact body in one step. We shall be specifically interested in situations where the size of the body is much larger than the spacing L of the faults.

Suppose that we wish to determine the stable configurations of the body. To this end, we introduce the potential energy

$$I(\boldsymbol{u}) = \int_\Omega W(\nabla \boldsymbol{u})\, dV + G(\boldsymbol{u}) \equiv F(\boldsymbol{u}) + G(\boldsymbol{u}) \tag{58}$$

where Ω is the domain of analysis; $\boldsymbol{u}$ is the displacement field; dV is the element of volume; and $G(\boldsymbol{u})$ is a loading term, e. g.,

$$G(\boldsymbol{u}) = \int_\Omega \rho \boldsymbol{B} \cdot \boldsymbol{u}\, dV + \int_{\partial\Omega_2} \bar{\boldsymbol{T}} \cdot \boldsymbol{u}\, dS \tag{59}$$

where $\rho\boldsymbol{B}$ is a body-force density per unit undeformed volume; $\bar{\boldsymbol{T}}$ are applied tractions per unit undeformed area; $\partial\Omega_2$ is the traction boundary; and dS is the corresponding element of area. We identify the stable configurations of the body with the configurations of minimum potential energy. In this manner we are led to the minimum problem

$$\inf_{\boldsymbol{u}\in X} I(\boldsymbol{u}) \tag{60}$$

where X is the configurational space of the body. For instance, an appropriate configuration space is $X = \{\boldsymbol{u} \in W^{1,\infty}(\Omega),\ \boldsymbol{u} = \bar{\boldsymbol{u}} \text{ on } \partial\Omega_1\}$, where $W^{1,\infty}(\Omega)$ is

the space of Lipschitz continuous functions; $\partial\Omega_1 = \partial\Omega - \partial\Omega_2$ is the displacement boundary; and $\bar{\boldsymbol{u}}$ is a prescribed boundary displacement function over $\partial\Omega_1$.

We begin by considering the limiting case of frictionless sliding. In this limit, and for a single level of faulting, the strain energy density can be expressed in the form:

$$W(\boldsymbol{F}) = \inf\{W^e(\boldsymbol{F}^e) + W^p(\boldsymbol{F}^p) : \boldsymbol{F} = \boldsymbol{F}^e\boldsymbol{F}^p\} \tag{61}$$

where

$$W^p(\boldsymbol{F}^p) = \begin{cases} f(|\boldsymbol{a}\cdot\boldsymbol{b}|, |\boldsymbol{a}\times\boldsymbol{b}|) & \text{if } \boldsymbol{F}^p = \boldsymbol{I} + \boldsymbol{a}\otimes\boldsymbol{b}\,, \quad \boldsymbol{a}\cdot\boldsymbol{b} \geq 0\,, \\ \infty & \text{otherwise} \end{cases} \tag{62}$$

The elastic energy satisfies

$$W^e(\boldsymbol{F}) = \infty, \text{ if } \det\boldsymbol{F} \leq 0\,, \tag{63a}$$
$$W^e(\boldsymbol{F}) < \infty, \text{ if } \det\boldsymbol{F} > 0\,, \tag{63b}$$

and is continuous on the set $\{\boldsymbol{F} : \det\boldsymbol{F} > 0\}$. In addition, the function f is continuous, nonnegative, vanishes at the origin and has sublinear growth, in the sense that

$$\lim_{t\to\infty} \frac{f(t\boldsymbol{x})}{|t|} = 0\,, \tag{64}$$

for all $\boldsymbol{x} \in \mathbb{R}^2$.

The preceding form of the energy density affords a number of revealing analogies to other models. Thus, within a variational framework of plasticity ([40]), (61) and (62) are in analogy to Tresca models of plasticity, in which yielding is assumed to occur instantaneously on a single–but otherwise arbitrary–slip system. However, an important difference between the present model and Tresca plasticity is that the faults are allowed to open in addition to sliding. Thus, in (62) the faulting model requires that $\boldsymbol{a}\cdot\boldsymbol{b} \geq 0$, whereas Tresca plasticity requires that $\boldsymbol{a}\cdot\boldsymbol{b} = 0$, corresponding to a deformation of pure slip. These differences notwithstanding, within the analogy to variational plasticity the assumption (64) of sublinear growth corresponds to an assumption of *strain softening*. On the strength of this analogy, we expect the static problem (60) to be highly degenerate. In particular, we expect the material to lose its bearing capacity in shear under conditions of all-around confinement; and to have no resistance to tensile fracture, or toughness. This latter property makes local softening models poor models of tensile fracture in general.

These expectations are rigorously born out by an investigation of the *relaxation* of the potential energy functional $I(\boldsymbol{u})$. This functional is not lower semicontinuous, and minimizing sequences form fine-scale oscillations. The aim then is to obtain the relaxation $J(\boldsymbol{u})$ of $I(\boldsymbol{u})$, which describes the macroscopic material behavior averaged over such fine scale structures. We recall that $J(\boldsymbol{u})$ is characterized by the two properties

(1) *Lower bound*. For each sequence $\boldsymbol{u}_h$ converging to $\boldsymbol{u}$,

$$J(\boldsymbol{u}) \leq \liminf_{h\to\infty} I(\boldsymbol{u}_h)$$

(2) *Recovery sequence*. For every $\boldsymbol{u}$ there is a sequence $\boldsymbol{u}_h$ converging to $\boldsymbol{u}$ such that

$$J(\boldsymbol{u}) = \lim_{h\to\infty} I(\boldsymbol{u}_h)\,.$$

Here convergence is understood in the sense of the weak-$W^{1,\infty}$ topology, i. e., we say that the sequence $\boldsymbol{u}_h$ converges to $\boldsymbol{u}$ if $\{\boldsymbol{u}_h\}$ is uniformly Lipschitz and $\boldsymbol{u}_h$ converges uniformly to $\boldsymbol{u}$. Standard theory shows that, if W is continuous,

$$J(\boldsymbol{u}) = \int_\Omega W^{\mathrm{qc}}(\nabla \boldsymbol{u})dV + G(\boldsymbol{u}) \tag{65}$$

where

$$W^{\mathrm{qc}}(\boldsymbol{F}) = \inf_{\boldsymbol{v}\in W_0^{1,\infty}(E)} \frac{1}{|E|}\int_E W(F+\nabla \boldsymbol{v})dV \tag{66}$$

is the *quasi-convex* envelope of W. Here $E \subset \mathbb{R}^3$ is any open set with Lipschitz boundary, and $W_0^{1,\infty}(E)$ is the space of Lipschitz continuous functions which vanish on the boundary ∂E. A scaling and covering argument shows that the definition of $W^{\mathrm{qc}}(\boldsymbol{F})$ does not depend on the choice of the domain E.

Standard theory also provides a compelling connection between the minimizers of $J(\boldsymbol{u})$ and $I(\boldsymbol{u})$. In particular, $\inf_{\boldsymbol{u}\in X} I(\boldsymbol{u}) = \inf_{\boldsymbol{u}\in X} J(\boldsymbol{u})$ and every cluster point of a minimizing sequence of $I(\boldsymbol{u})$ is a minimum point of $J(\boldsymbol{u})$. Conversely, every minimum point of $J(\boldsymbol{u})$ is the limit of a minimizing sequence of $I(\boldsymbol{u})$ in X. The relaxed functional $J(\boldsymbol{u})$ is always lower semi-continuous. If $I(\boldsymbol{u})$ is coercive, then $J(\boldsymbol{u})$ is also coercive and, hence, has a minimum point in X. These properties of relaxation show that the functional $I(\boldsymbol{u})$ can be replaced by the better-behaved functional $J(\boldsymbol{u})$ without essential loss of information. The minimizing sequences of $I(\boldsymbol{u})$ then correspond to *microstructures* and minimizers of $J(\boldsymbol{u})$ characterize their average properties. For a precise exposition of these and related concepts, see e. g., [21, Sect. 5.2] and [26, Sect. 4].

In the present setting, the functional $I(\boldsymbol{u})$ is not coercive and, therefore, existence cannot be guaranteed in general even for the relaxed functional. This degeneracy, which is illustrated by the examples after Proposition 1, owes to the lack of macroscopic resistance to tension and slip (cf also the discussion below). Further, since the energy density W under consideration incorporates a positive-determinant constraint the general results that link the relaxed functional to the quasiconvex envelope W^{qc} hold for C^1 displacement fields $\boldsymbol{u}$ only.

Our main result is a characterization of the quasiconvex envelope of W.

Proposition 1 *The quasiconvex envelope of W, defined in (61-64), is:*

$$W^{\rm qc}(\boldsymbol{F}) = \varphi^{**}(\det \boldsymbol{F}) \tag{67}$$

where φ^{**} is the convex envelope of the function

$$\varphi(t) = \inf \{W^e(\boldsymbol{F}^e) : \ \det \boldsymbol{F}^e \leq t\} \ . \tag{68}$$

The proof of this proposition is given in the appendix. To illustrate the significance of this result, we provide two explicit examples.

Example 1: Suppose that $W^e(\boldsymbol{F}) = \mathrm{dist}^2(\boldsymbol{F}, SO(3)) + \psi(\det \boldsymbol{F})$ for some convex nonnegative ψ with $\psi(1) = 0$ and $\psi(t) = \infty$ for $t < 0$. Since

$$\mathrm{dist}^2(\boldsymbol{F}, SO(3)) = \sum_{i=1}^{3} (\lambda_i(\boldsymbol{F}) - 1)^2 \, , \tag{69}$$

where $\lambda_i(\boldsymbol{F})$ are the singular values of $\boldsymbol{F}$, we get

$$\inf \{W^e(\boldsymbol{F}) : \ \det \boldsymbol{F} = t\} = 3(t^{1/3} - 1)^2 + \psi(t) \, . \tag{70}$$

Then it follows that

$$\varphi^{**}(t) = \varphi(t) = \begin{cases} \infty & \text{if } t < 0 \\ 3(t^{1/3} - 1)^2 + \psi(t) & \text{if } 0 \leq t < 1 \\ 0 & \text{if } t \geq 1 \, . \end{cases} \tag{71}$$

□

Example 2: Let $W^e(\boldsymbol{F}) = W^{\rm dev}(\boldsymbol{F}^{\rm dev}) + \psi(\det \boldsymbol{F})$, with ψ as above, $\boldsymbol{F}^{\rm dev} \equiv (\det \boldsymbol{F})^{-1/3} \boldsymbol{F}$, $W^{\rm dev}$ nonnegative and $W^{\rm dev}(\boldsymbol{I}) = 0$. Then

$$\inf \left\{ W^{\rm dev}(\boldsymbol{F}^{\rm dev}) : \ \det \boldsymbol{F} = t \right\} = 0 \tag{72}$$

for any $t \neq 0$, e. g., by choosing $\boldsymbol{F} = t^{1/3} \boldsymbol{I}$. Therefore

$$\varphi(t) = \inf \{\psi(s) : \ s \leq t\} \ , \tag{73}$$

and, consequently,

$$\varphi^{**}(t) = \varphi(t) = \begin{cases} \infty & \text{if } t < 0 \\ \psi(t) & \text{if } 0 \leq t < 1 \\ 0 & \text{if } t \geq 1 \, . \end{cases} \tag{74}$$

□

Proposition 1 can be readily extended to polycrystals. To this end, suppose that the domain Ω is subdivided into countably many Lipschitz subsets ω_i with an orientation $\boldsymbol{Q}_i \in SO(3)$ ascribed to each subset. The corresponding strain energy is

$$I(\boldsymbol{u}) = \sum_i \int_{\omega_i} W(\nabla \boldsymbol{u}\boldsymbol{Q}_i) dV \tag{75}$$

Then, an application of Proposition 1 to each grain yields the following result.

Corollary 2 *The relaxation of $I(\boldsymbol{u})$, eq. (75), is given on maps $\boldsymbol{u} \in C^1(\Omega, \mathbb{R}^3)$ by the isotropic functional*

$$J(\boldsymbol{u}) = \int_\Omega W^{\rm qc}(\nabla \boldsymbol{u}) dV \,. \tag{76}$$

The preceding results shed considerable light into the properties of the quasistatic problem (60) defined by the local and frictionless recursive faulting model. Thus, proposition 1 and the subsequent examples show that, for a broad range of commonly assumed elastic energy densities, the effective behavior of the material falls into two well-differentiated regimes: the *compressive regime*, $\det \boldsymbol{F} < 1$, corresponding to strong all-around confinement; and the *tensile regime*, $\det \boldsymbol{F} > 1$, characterized by the presence of directions of large tensile deformation. In the compressive regime, the material retains is volumetric load-bearing capacity but loses its shear load-bearing capacity completely. In the tensile regime, the material disintegrates completely. It is interesting to note that, as shown in the appendix, recursive faulting does indeed provide a class of minimizing sequences that delivers the relaxation of the material, which justifies the recursive faulting construction described in § 2.7.

In practice there are several sources of regularizaton that prevent the attainment of the degenerate limit just described. Firstly, relaxation represents a highly idealized limit that is attained only if the material is capable of exploring all possible microstructures. A more common type of physical behavior is *metastability*, in which the system falls in local minima instead of attaining the infimum of the energy. Other common sources of regularization are viscosity and dynamics [43; 44]. In the present context the role of viscosity, albeit rate-independent, is played by friction. In this case, the sublinear growth (64) is replaced by linear growth and the material no longer exhibits softening. The relaxation of the resulting energy is beyond the scope of this paper, but may be expected to be similar to that of other models having linear growth, including single-crystal plasticity [35]. Finally, in a time-discretized framework the effect of inertia is to add an L^2-continuous quadratic positive-definite term to the incremental energy functional [43; 44]. The resulting stabilizing effect of inertia in otherwise non-convex problems has been investigated by Dolzmann and Friesecke [43] and Demoulini [45]. However, even allowing for metastability and frictional and dynamical regularization the relaxation result of proposition 1 does provide useful information about the general trends in the expected macroscopic behavior, such as the existence of well-differentiated

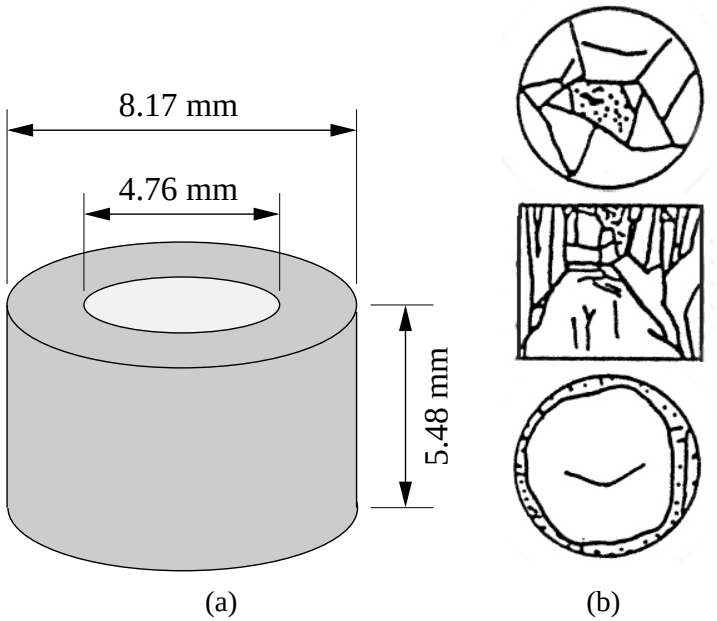

Fig. 4. (a) Geometry of the sleeved specimen used in the experiments of Chen and Ravichandran [2; 4]. Internal diameter 4.76 mm, external diameter 8.17 mm, height 5.48 mm. (b) Schematic of the damage patterns in the confined specimen at the end of the experiment (Fig. 8 in [2]), from top to bottom: top view, vertical cross section, and bottom view.

compressive and tensile regimes.

4 Validation examples

As an example of application of the recursive faulting model, and by way of validation, we proceed to simulate the dynamic multi-axial compression experiments on sintered aluminum nitride (AlN) of Chen and Ravichandran [1; 2; 3; 4]. Chen and Ravichandran's experimental technique is designed for imposing controlled lateral confinement on specimens subjected to dynamic uniaxial compression [1; 3]. In Chen and Ravichandran's experiments, an axial compression is applied by a split Hopkinson pressure bar modified to subject the specimen to a single loading pulse during the experiment. The specimen is confined laterally by a shrink-fit metal sleeve, Fig. 4a. We specifically focus on Chen and Ravichandran's data for for aluminum nitride (AlN) [2; 4]. The experiments provide a wealth of validation data, including loading histories, the axial stress-strain curves, as well as detailed crack patterns in the confined specimen, Fig. 4b. The data show that failure occurs by fragmentation due to axial splitting under uniaxial stress conditions; and by localized shear deformation under moderate lateral confinement. The compressive failure strength of ceramic materials increases with increasing confinement pressure. It is also observed that the propensity for ceramics to fragment is suppressed by lateral confinement. Furthermore, ceramics exhibit some inelasticity in the stress-

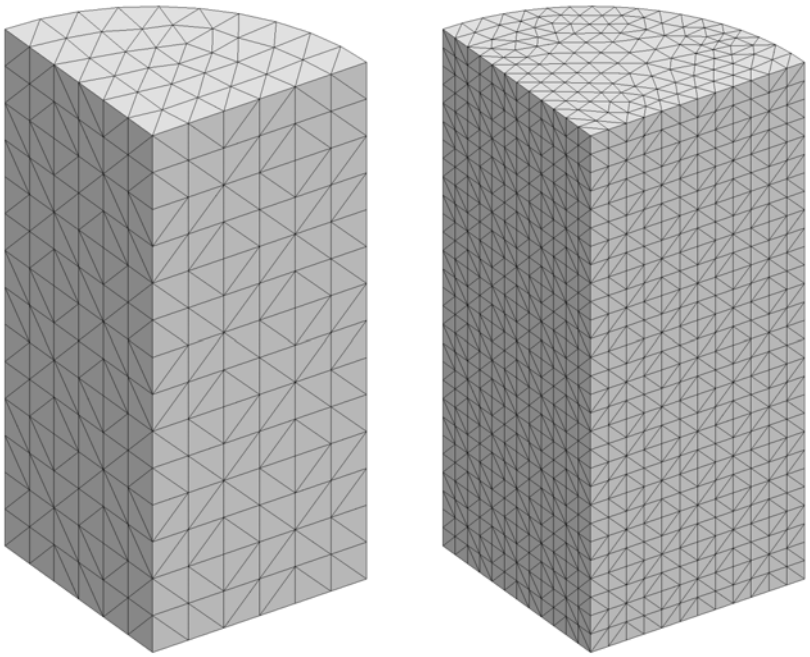

(a) (b)

Fig. 5. Finite element meshes used in the calculations (a) Coarse 217-elements mesh; and (b) fine 2004-elements mesh.

strain behavior in the presence of lateral confinement.

The material properties of AlN used in the calculations are collected in Table 2. The elastic modulus E, the Poisson coefficient ν and the mass density ρ are reported in [2]. The tensile strength T_c is chose in the middle of the experimental range of 155-214 MPa characteristic of structural ceramics [46]. The coupling parameter β is estimated from the difference between tensile and compressive strengths of the material. The critical opening displacement Δ_c is estimated from static data. From the top view of the observed damage pattern, Fig. 4b, the distribution of rank-1 faults is assumed to be coarse and, in consequence, the fault separation L is taken to be one half of the specimen diameter.

E (GPa)	ν	T_c (MPa)	Δ_c (μm)	β	L (mm)	μ	ρ (kg/m^3)
310	0.237	180	1.8	3.464	2.38	0.25	3200

Table 2. AlN material constants adopted in the calculation.

The AlN specimen under consideration is 4.76 mm in diameter and 5.48 mm in length, Fig. 4a. The outer diameter of the sleeve is 8.17 mm, and the inner diameter is 0.025 mm less than the specimen diameter. The specimen is loaded by imposing the experimentally recorded velocity profile (Fig. 4, [2]) on the side of

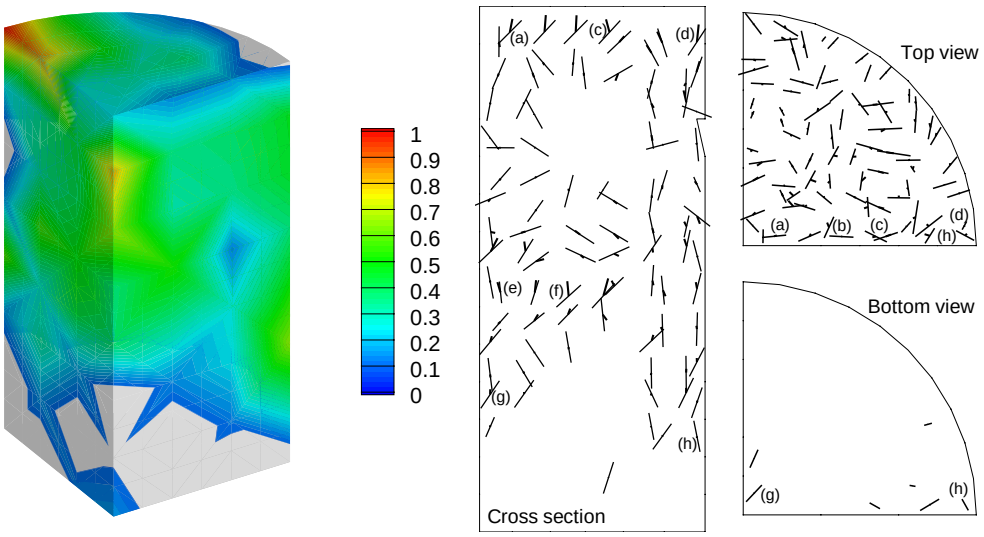

(a) (b)

Fig. 6. Numerical simulation of the confined specimen allowing for rank-1 faulting only. a) Computed contour levels of damage in rank-1 faulting calculations. The damage variable ranges from 0 to 1 and represents the fraction of specific fracture energy expended by the material. b) Cross section, top view and bottom view of the fault distribution. The lines represent the fault planes and the arrows the opening displacement vector. The fault structures labelled (a)-(h) are shown in Fig. 7.

the incident bar. For simplicity, we consider the limiting cases of and unconfined specimen, corresponding to a traction-free lateral surface; and rigid confinement, corresponding to constraining the radial displacement of the lateral surface. Owing to the symmetry of the problem we may model one fourth of the specimen only. In order to investigate matters of mesh-size dependency we consider two meshes: a course mesh consisting of 217 10-node tetrahedral finite elements (504 nodes); and a second finer mesh consisting of 2004 10-node tetrahedra and 3428 nodes. The geometry of the sleeve-core assembly and the two meshes used in the simulations are shown in Fig. 4a and 5, respectively.

The results of a first set of simulations of the confined case obtained by allowing rank-1 faulting only are shown in Figs. 6, 7 and 8. Fig. 6 shows the general distribution of damage at the end of the simulation of the confined case. Damage is represented by means of a damage parameter defined as the ratio between the energy expended in fracture and the specific fracture energy of the material. By virtue of this definition, the damage parameter ranges from 0 for the undamaged material to 1 for fully developed cracks in tension or shear. In the confined case the computed distribution of damage exhibits characteristic cone failure and a region of extensive compressive damage, or crushing, under the front surface of the specimen, Fig. 6, in general agreement with experiment, Fig. 4b. The detailed orientation and activity of the faults is shown in Fig. 6b. The rank-1 faulting microstructures that develop at selected material points are shown in Fig. 7. The computed faults in the crushing

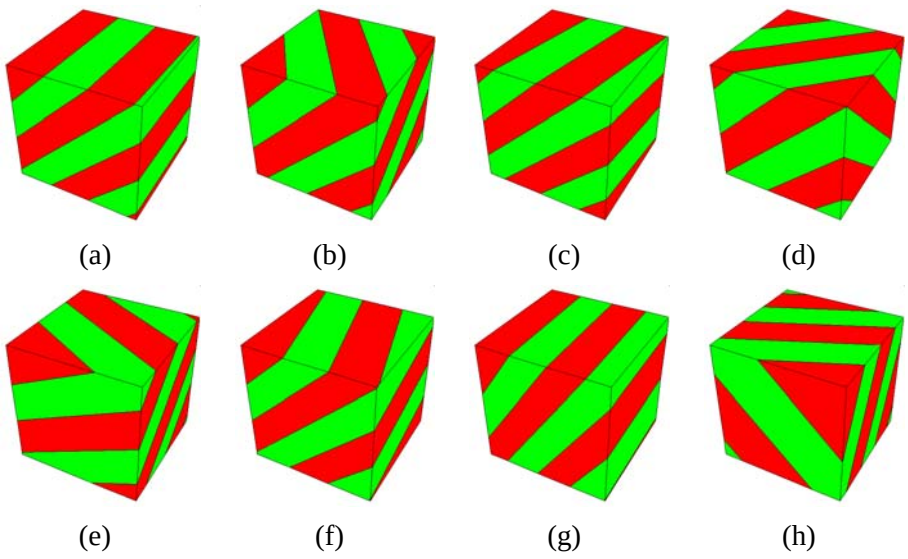

Fig. 7. Numerical simulation of the confined specimen allowing for rank-1 faulting only. Detailed view of rank-1 fault structures computed at points (a)-(h) of Fig. 6b.

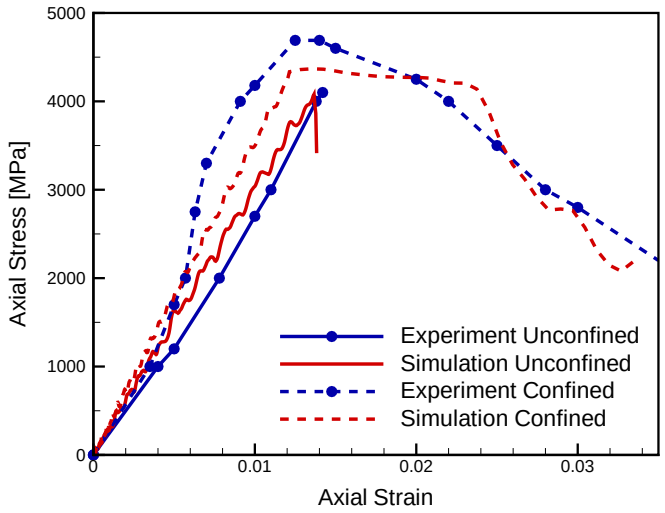

Fig. 8. Numerical simulation of the confined specimen allowing for rank-1 faulting only. Experimental and predicted axial stress *vs.* axial strain curves.

zone tend to align vertically, specially in the periphery of the specimen, but do not exhibit a preferred orientation on cross section of the specimen normal to the axis. These trends are generally consistent with the observed fracture patterns, Fig. 4b.

In the simulations of the unconfined case, intense damage occurs over vast regions of the specimen, especially in the vicinity of the posterior surface. Deformation trapping at the boundary is known to occur in one-dimensional wave propagation through softening materials ([47]). Comparison of fracture patterns with experiment is not possible in this case since the specimen was not recovered.

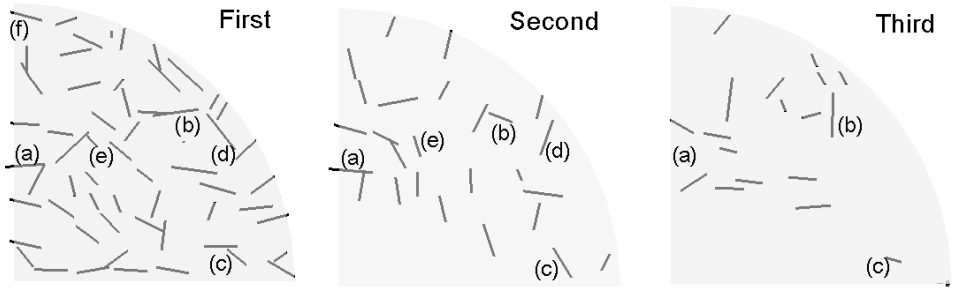

Fig. 9. Numerical simulation of the confined specimen allowing for rank-3 recursive faulting. Top view of the first, second and third-level fault distribution. Fault structures at points labelled (a)-(f) are shown in Fig. 10.

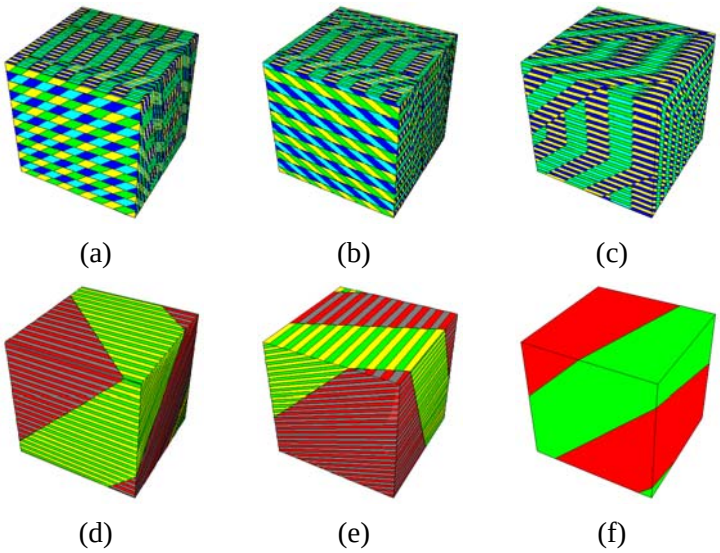

Fig. 10. Numerical simulation of the confined specimen allowing for rank-3 recursive faulting. Detailed view of recursive faulting structures computed at points (a)-(h) of Fig. 9. (a)-(c) Rank-3 microstructures. (d)-(e) Rank-2 microstructures. (f) Rank-1 microstructure.

Fig. 8 shows the plots of axial stress *vs.* axial strain for the unconfined and confined cases. The figure also shows the corresponding experimental data for comparison. The sharp contrast between the unconfined and confined cases is immediately apparent in the figure. Thus, in the unconfined case the specimen fails catastrophically upon the attainment of the tensile strength of the material. Subsequent to the failure point, the load-bearing capacity of the specimen drops precipitously. By way of contrast, the confined specimen exhibits quasi-ductile behavior. Indeed, following the point of inception of damage the specimen enters a yielding regime, though it eventually strain-softens and fails. Thus, the addition of confinement alters the behavior of the specimen from perfectly brittle to quasi-ductile, an effect that may be thought of as a *brittle-to-ductile transition*. These predicted general trends are also clearly visible in the experimental curves. The ability of the model to predict the transition from perfectly brittle to quasi-ductile behavior resulting from the addition of confinement is particularly noteworthy.

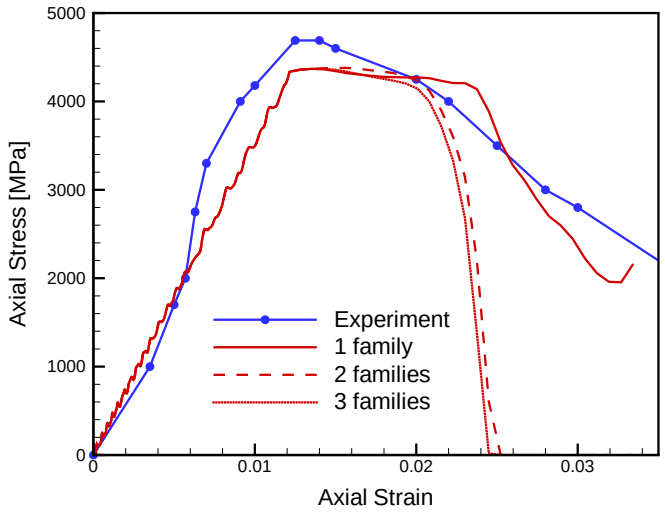

Fig. 11. Numerical simulation of the confined specimen allowing for rank-3 recursive faulting. Experimental and predicted axial stress *vs.* axial strain curves.

The results of numerical simulation allowing for rank-3 recursive faulting microstructures are shown in Fig. 9, 10 and 11. Fig. 9 shows that rank-1 microstructures are the most common, with rank-2 and rank-3 microstructures arising with diminishing frequency. In addition, complex recursive fault patterns of rank higher than one develop primarily in the vicinity of the anterior surface of the specimen, and become increasingly rare with depth in the axial direction. This concentration of damage may again be regarded as an instance of deformation trapping ([47]). The intricate patterns of damage and deformation that correspond to rank-2 and rank-3 microstructures are shown in Fig. 10 at selected sampling points. The ability of the model to general complex sub-grid microstructures *on the fly* as part of a macroscopic finite-element calculation is noteworthy. In order to calculate the separations at all levels of faulting, we take the compliance C in (52) to be of the order of the shear modulus; and the 'core cut-off' distance L_0 to be of the order of $100\Delta_c$. The resulting fault separations are: 2.38, 0.09 and 0.24 mm, corresponding to levels one, two and three, respectively. The effect of recursive faulting on the macroscopic stress-strain curve is to soften the post-peak response and accelerate failure, Fig. 11, partly owing to damage concentration and deformation trapping at the boundary.

Finally, Fig. 12 shows a comparison of results corresponding to the coarse and fine meshes depicted in Fig. 5. The calculations concern the confined specimen and allow for rank-1 faulting only. The comparison demonstrates the mesh-size independence of the calculations. This mesh-size independence is expected since, under sufficient confinement, damage takes place in a distributed fashion and does not exhibit localization. This diffuse nature of compressive damage in turn owes to the stabilizing effect of inertia and internal friction, as remarked in § 3.

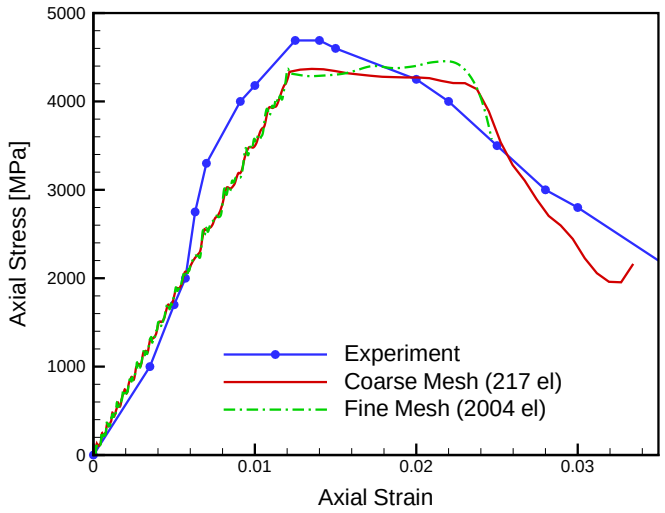

Fig. 12. Axial stress *vs.* axial strain curves for confined specimens using the meshes shown in Fig. 5.

5 Summary and concluding remarks

We have developed a model of distributed damage in brittle materials deforming in triaxial compression based on the explicit construction of special microstructures. These microstructures are obtained by *recursive faulting*, i. e., by recursively fitting faults within faults. The model accounts for the elasticity of the matrix, fault nucleation and the cohesive and frictional behavior of the faults. We have also developed a time discretization of the model that confers the incremental problem a variational structure. We resort to this variational structure in order to predict the inception of the faults and their optimal orientation and separation. We also exploit the variational structure of the incremental quasistatic boundary-value problem for purposes of mathematical analysis and determine the relaxation of the potential energy, which describes the macroscopic material behavior averaged over all possible fine-scale structures. This analysis delineates two well-differentiated regimes in the macroscopic behavior of the material: a *compressive regime*, in which the material retains is volumetric load-bearing capacity but tends to lose its shear load-bearing capacity completely; and the *tensile regime*, in which the material tends to disintegrate completely. Finally, we present numerical calculations of the dynamic multi-axial compression experiments on sintered aluminum nitride (AlN) of Chen and Ravichandran [1; 2; 3; 4]. In this calculations, the microstructure is not resolved by the mesh and is modelled at the sub-grid level. Specifically, the recursive faulting construction is used to generate sub-grid microstructures 'on the fly' as part of a finite-element analysis. In this sense, the approach provides an example of *concurrent multiscale computing*, i. e., of a computational scheme in which two or more length scales are carried simultaneously within the same calculation. The model correctly predicts the general trends regarding the observed damage patterns; and

the brittle-to-ductile transition resulting under increasing confinement.

In closing, we point to some of the limitations of the model and related open questions. Firstly, it should be carefully noted that the model makes sense under conditions resulting in diffuse or distributed damage. Our analysis and numerical experiments indicate that these conditions are met in triaxial compression under sufficiently strong confinement, specifically, when $\det(\boldsymbol{F}) < 1$. Under strongly tensile conditions, i. e., when $\det(\boldsymbol{F}) > 1$, localization into a small number of dominant cracks is to be expected and the model ceases to apply. Indeed, damage or softening models are poor models of fracture in general, as they lack a specific fracture energy per unit surface, and a model of discrete fracture is preferable in that regime. We also expect the presence of friction to modify substantially the relaxation of the model. In particular, friction may be expected to confer the material resistance to macroscopic shearing deformation in compression. However, the relaxation of the frictional model is unknown to us at present. Moreover, there is a paucity of mathematical tools for characterizing the macroscopic behavior of solids with microstructure in the presence of inertia. In addition, the question of kinetics of fault nucleation appears to be open at present as well.

Acknowledgements

MO and AP gratefully acknowledge the support of the Department of Energy through Caltech's ASCI ASAP Center for the Simulation of the Dynamic Response of Materials. AP additionally acknowledges the support of the Italian MIUR through the Cofin2003 program "Interfacial damage failure in structural systems: applications to civil engineering and emerging research fields". The work of SC was supported by the Deutsche Forschungsgemeinschaft through the Schwerpunktprogramm 1095 *Analysis, Modeling and Simulation of Multiscale Problems*. This work was partially carried during MO's stay at the Max Planck Institute for Mathematics in the Sciences of Leipzig, Germany, under the auspices of the Humboldt Foundation. MO gratefully acknowledges the financial support provided by the Foundation and the hospitality extended by the Institute.

A Appendix: Proof of Proposition 1

We recall that the relaxation extends trivially in the presence of continuous perturbations such as body forces and boundary tractions (e. g., [48; 49]). Since, with the convergence criterion under consideration, $G(\boldsymbol{u})$ in (59) is continuous, we may therefore focus on the relaxation of the strain-energy $\boldsymbol{F}(\boldsymbol{u})$. The results thus obtained are immediately applicable to the general boundary value problem which

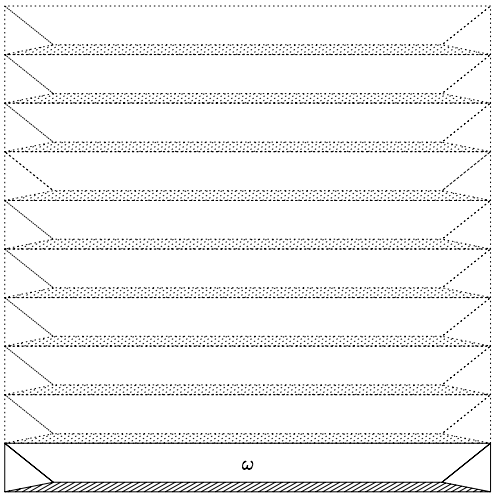

Fig. A.1. Sketch of the construction used to prove (A.1). The dashed area is the set S where the gradient $\boldsymbol{F}_k(\boldsymbol{I} + \varepsilon^{-1}\boldsymbol{a}_k \otimes \boldsymbol{b}_k)$ is used. The dotted parts are copies of R, and indicate the global construction that can be used in the unit square.

governs the quasistatic deformations of bodies subjected to body forces and displacement boundary conditions on part of $\partial\Omega$.

Proof. We claim that for any $k \in \mathbb{N}$ we have

$$\text{if } \boldsymbol{F} = \boldsymbol{F}^e \prod_{i=1}^{k} (\boldsymbol{I} + \boldsymbol{a}_i \otimes \boldsymbol{b}_i) \text{ with } \boldsymbol{a}_i \cdot \boldsymbol{b}_i \geq 0, \qquad \text{then } W^{\mathrm{qc}}(\boldsymbol{F}) \leq W^e(\boldsymbol{F}^e)\,. \tag{A.1}$$

We prove this claim by induction. If $k = 0$ there is nothing to prove. Assume the claim holds for some $k \geq 0$, and consider

$$\boldsymbol{F}_k = \boldsymbol{F}^e \prod_{i=1}^{k} (\boldsymbol{I} + \boldsymbol{a}_i \otimes \boldsymbol{b}_i)\,, \qquad \boldsymbol{F}_{k+1} = \boldsymbol{F}_k(\boldsymbol{I} + \boldsymbol{a}_{k+1} \otimes \boldsymbol{b}_{k+1})\,, \tag{A.2}$$

with all $\boldsymbol{a}_i \cdot \boldsymbol{b}_i \geq 0$. Without loss of generality we can assume $|\boldsymbol{b}_{k+1}| = 1$, and after a rotation $\boldsymbol{b}_{k+1} = \boldsymbol{e}_3$. Fix two small parameters ε and $\delta \in (0, 1)$, and consider in (66) the domain

$$E = (0, 1)^2 \times (0, \delta). \tag{A.3}$$

We shall prove the claim by constructing a suitable test function $\boldsymbol{v}$ on the domain E. Let $g : E \to \mathbb{R}$ be defined by

$$g(\boldsymbol{x}) = \begin{cases} x_3/\varepsilon & \text{if } x_3 \leq \varepsilon\delta \\ \delta & \text{if } x_3 \geq \varepsilon\delta\,, \end{cases} \tag{A.4}$$

and set

$$h(\boldsymbol{x}) = \min(g(\boldsymbol{x}), x_3 + \xi \mathrm{dist}(\boldsymbol{x}, \partial E))\,, \tag{A.5}$$

where ξ is a positive number smaller than $1/|a_{k+1}|$. We define

$$\boldsymbol{u}(\boldsymbol{x}) = \boldsymbol{F}_k\boldsymbol{x} + \boldsymbol{F}_k\boldsymbol{a}_k h(\boldsymbol{x})\,. \tag{A.6}$$

and compute

$$\nabla \boldsymbol{u}(\boldsymbol{x}) = \boldsymbol{F}_k + \boldsymbol{F}_k \boldsymbol{a}_k \otimes \nabla h(\boldsymbol{x})\,. \tag{A.7}$$

This gradient is constant in each of finitely many pieces of E (four in two dimensions, cf Fig. A.1; six in three dimensions), and it takes values $\boldsymbol{F}_k$, $\boldsymbol{F}_k(\boldsymbol{I} + \varepsilon^{-1}\boldsymbol{a}_{k+1}\otimes\boldsymbol{b}_{k+1})$, $\boldsymbol{F}_k(\boldsymbol{I}+\boldsymbol{a}_{k+1}\otimes(\boldsymbol{e}_3\pm\xi\boldsymbol{e}_1))$, $\boldsymbol{F}_k(\boldsymbol{I}+\boldsymbol{a}_{k+1}\otimes(\boldsymbol{e}_3\pm\xi\boldsymbol{e}_2))$, which all have positive determinant. The function $\boldsymbol{u}(\boldsymbol{x})$ is Lipschitz continuous, and equals $F_{k+1}\boldsymbol{x}$ on ∂E. Let ω be the subset of E where $\nabla\boldsymbol{u} = \boldsymbol{F}_k$. By the inductive assumption, $W^{\mathrm{qc}}(\boldsymbol{F}_k) \le W^e(\boldsymbol{F}^e)$, hence (using the definition (66) on the domain ω), for any $\eta > 0$ there is a Lipschitz continuous function $\boldsymbol{v}' : \omega \to \mathbb{R}^3$ such that

$$\boldsymbol{v}'(\boldsymbol{x}) = \boldsymbol{F}_k\boldsymbol{x} \text{ on } \partial\omega\,, \quad \text{and} \quad \frac{1}{|\omega|}\int_\omega W(\nabla\boldsymbol{v}')dV \le W^e(\boldsymbol{F}^e) + \eta\,. \tag{A.8}$$

We define $\boldsymbol{w} : E \to \mathbb{R}^3$ by

$$\boldsymbol{w}(\boldsymbol{x}) = \begin{cases} \boldsymbol{v}'(\boldsymbol{x}) & \text{if } \boldsymbol{x} \in \omega\,, \\ \boldsymbol{u}(\boldsymbol{x}) & \text{if } \boldsymbol{x} \in E\setminus\omega\,. \end{cases} \tag{A.9}$$

The function $\boldsymbol{w}$ is Lipschitz continuous, and $\boldsymbol{w}(\boldsymbol{x}) = \boldsymbol{F}_{k+1}\boldsymbol{x}$ on ∂E. Therefore $\boldsymbol{v}(\boldsymbol{x}) = \boldsymbol{w}(\boldsymbol{x}) - \boldsymbol{F}_{k+1}\boldsymbol{x} \in W^{1,\infty}_0(E)$ and, from the definition (66), we have

$$W^{\mathrm{qc}}(\boldsymbol{F}_{k+1}) \le \frac{1}{|E|}\int_E W(\boldsymbol{F}_{k+1}+\nabla\boldsymbol{v})dV = \frac{1}{|E|}\int_E W(\nabla\boldsymbol{w})dV\,. \tag{A.10}$$

It remains to evaluate the last integral. The contribution from ω is controlled by (A.8). On the rest the gradient $\nabla\boldsymbol{w} = \nabla\boldsymbol{u}$ takes only five distinct values, as mentioned above. The large gradient $\nabla\boldsymbol{u} = \boldsymbol{F}_k(\boldsymbol{I} + \varepsilon^{-1}\boldsymbol{a}_{k+1}\otimes\boldsymbol{b}_{k+1})$ is taken only in a thin strip $S \subset (0,1)^2\times(0,\varepsilon\delta)$, which has volume controlled by $|S| \le \varepsilon|E|$. The corresponding energy is controlled by

$$\int_S W(\nabla\boldsymbol{w})dV \le |E|\varepsilon\left[W^e(\boldsymbol{F}_k) + f\left(\frac{1}{\varepsilon}\boldsymbol{a}_{k+1}\cdot\boldsymbol{b}_{k+1}, \frac{1}{\varepsilon}|\boldsymbol{a}_{k+1}\times\boldsymbol{b}_{k+1}|\right)\right]\,. \tag{A.11}$$

By (64), we get

$$\lim_{\varepsilon\to 0}\varepsilon\left[W^e(\boldsymbol{F}_k) + f\left(\frac{1}{\varepsilon}\boldsymbol{a}_{k+1}\cdot\boldsymbol{b}_{k+1}, \frac{1}{\varepsilon}|\boldsymbol{a}_{k+1}\times\boldsymbol{b}_{k+1}|\right)\right] = 0\,, \tag{A.12}$$

hence we can choose ε sufficiently small so that the integral in (A.11) is less than $|E|\eta$. The remaining pieces are located close to the short sides of E, and have the form of closure domains (see Figure A.1). Their volume is controlled by is $\delta|E|$, and $\boldsymbol{F}$ there takes the four values $\boldsymbol{F}_k(\boldsymbol{I} + \boldsymbol{a}_{k+1}\otimes(\boldsymbol{e}_3 \pm \xi\boldsymbol{e}_{1,2}))$, which do not depend on ε and δ. Therefore we can choose δ so that

$$\begin{aligned}&\delta|E|W^e\left(\boldsymbol{F}_k(\boldsymbol{I}+\boldsymbol{a}_{k+1}\otimes(\boldsymbol{e}_3\pm\xi\boldsymbol{e}_1))\right)\\ &\quad+\delta|E|W^e\left(\boldsymbol{F}_k(\boldsymbol{I}+\boldsymbol{a}_{k+1}\otimes(\boldsymbol{e}_3\pm\xi\boldsymbol{e}_2))\right) \le \eta\,.\end{aligned} \tag{A.13}$$

We conclude that

$$W^{\rm qc}(\boldsymbol{F}_{k+1}) \leq \frac{1}{|E|}\int_\omega W(\nabla \boldsymbol{w})dV + 3\eta \leq W^e(\boldsymbol{F}^e) + 4\eta \tag{A.14}$$

which, since η was arbitrary, proves the claimed (A.1).

It remains to be shown that (A.1) implies the thesis. This follows from the fact that any matrix of unit determinant can be written as product of simple shears of the form $\boldsymbol{I} + \lambda \boldsymbol{e}_i \otimes \boldsymbol{e}_j$, with $i \neq j$ and $\lambda \in \mathbb{R}$ (to see this, just consider that multiplying $\boldsymbol{F}$ by $\boldsymbol{I} + \lambda \boldsymbol{e}_i \otimes \boldsymbol{e}_j$ on the left corresponds to adding a multiple of the i-th column to the j-th one, and multiplying on the right does the same on rows. Therefore the claim is equivalent to Gauss reduction). We conclude that given any pair of matrices $\boldsymbol{F}$, $\boldsymbol{F}^e$ with $0 < \det \boldsymbol{F}^e \leq \det \boldsymbol{F}$, one can find vectors $\boldsymbol{a}_i$ and $\boldsymbol{b}_i$ with $\boldsymbol{a}_i \cdot \boldsymbol{b}_i \geq 0$ such that

$$\boldsymbol{F} = \boldsymbol{F}^e \prod_{i=1}^{k} (\boldsymbol{I} + \boldsymbol{a}_i \otimes \boldsymbol{b}_i)\,. \tag{A.15}$$

Then, the claim (A.1) implies that

$$W^{\rm qc}(\boldsymbol{F}) \leq W^e(\boldsymbol{F}^e) \qquad \text{for all } \boldsymbol{F}^e \text{ with } \det \boldsymbol{F}^e \leq \det \boldsymbol{F}\,. \tag{A.16}$$

We conclude

$$W^{\rm qc}(\boldsymbol{F}) \leq \varphi(\det \boldsymbol{F})\,, \tag{A.17}$$

where φ was defined in (68). Consider now a matrix $\boldsymbol{F}$, and view it as the average of

$$\boldsymbol{F}_\pm = \boldsymbol{F}\left(\boldsymbol{I} \pm \frac{1}{2}\boldsymbol{e}_1 \otimes \boldsymbol{e}_1\right)\,. \tag{A.18}$$

By lamination it follows that

$$W^{\rm qc}(\boldsymbol{F}) \leq \frac{W^{\rm qc}(\boldsymbol{F}_+) + W^{\rm qc}(\boldsymbol{F}_-)}{2} \leq \frac{1}{2}\left[\varphi\left(\frac{3}{2}\det \boldsymbol{F}\right) + \varphi\left(\frac{1}{2}\det \boldsymbol{F}\right)\right]\,, \tag{A.19}$$

and the same can be done with any other weight. This shows that

$$W^{\rm qc}(\boldsymbol{F}) \leq \varphi^{**}(\det \boldsymbol{F})\,. \tag{A.20}$$

But $\varphi^{**}(\det \boldsymbol{F})$ is polyconvex function, and $\varphi^{**}(\det \boldsymbol{F}) \leq W(\boldsymbol{F})$, hence equality holds. □

References

[1] W. Chen and G. Ravichandran. Dynamic compressive behavior of ceramics under lateral confinement. *Journal de Physique IV*, 4:177–182, 1994.

[2] W. Chen and G. Ravichandran. Static and dynamic compressive behavior of aluminum nitride under moderate confinement. *Journal of the American Society of Ceramics*, 79(3):579–584, 1996.

[3] W. Chen and G. Ravichandran. An experimental technique for imposing dynamic multiaxial compression with mechanical confinement. *Experimental Mechanics*, 36(2):155–158, 1996.

[4] W. Chen and G. Ravichandran. Failure mode transition in ceramics under dynamic multiaxial compression. *International Journal of Fracture*, 101:141–159, 2000.

[5] J. Lemaitre. How to use damage mechanics. *Nuclear Engineeering Design*, 80:233–245, 1984.

[6] M. Ortiz. A constitutive theory for the inelastic behavior of concrete. *Mechanics of Materials*, 4:67–93, 1985.

[7] Z. P. Bazant. Mechanics of distributed cracking. *Applied Mechanical Reviews, ASME*, 39:675–705, 1986.

[8] Z. P. Bazant and G. Pijaudier-Cabot. Nonlocal continuum damage, localization instability and convergence. *Journal of Applied Mechanics*, 55:287–293, 1988.

[9] J. Mazars and G. Pijaudier-Cabot. Continuum damage theory application to concrete. *ASCE - Journal of Engineering Mechanics*, 115:345–365, 1989.

[10] R. Talreja. Continuum modeling of damage in ceramic matrix composites. *Mechanics of Materials*, 12(2):165–180, 1991.

[11] Z. P. Bazant and M. Jirasek. Nonlocal model based on crack interactions: A localization study. 116:256–259, 1994.

[12] R. de Borst, J. Pamin, R. H. J. Peerlings, and L. J. Sluys. On gradient-enhanced damage and plasticity models for failure in quasi-brittle and frictional materials. *Computational Mechanics*, 17(1):130–141, 2001.

[13] Lyakhovsky V., Y. Ben-Zion, and Agnon A. Distributed damage, faulting, and friction. *Journal of Geophysical Research - Solid Earth*, 102:27635–27649, 1997.

[14] C. Comi. Computational modelling of gradient-enhanced damage in quasi-brittle materials. *Mechanics of Cohesive and Frictional Materials*, 4(1):17–36, 1999.

[15] Z. P. Bazant and M. Jirasek. Nonlocal integral formulations of plasticity and damage: survey of progress. *ASCE - Journal of Engineering Mechanics*, 128(11):1119–1149, 2002.

[16] E. De Giorgi, M. Carriero, and A. Leaci. Existence theorem for a minimum problem with free discontinuity set. *Archives of Rational Mechanics and Analysis*, 108:105–218, 1989.

[17] G. Francfort and J.-J. Marigo. Revisiting brittle fracture as an energy minimization problem. *Journal of Mechanics and Physics of Solids*, 46(8):1319–1342, 1998.

[18] G. Dal Maso, G. A. Francfort, and R. Toader. Quasistatic crack growth in nonlinear elasticity. *Archive for Rational Mechanics and Analysis*, 176(2):165–225, 2005.

[19] G. Dal Maso and R. Toader. A model for the quasi-static growth of brittle fractures: Existence and approximation results. *Archives of Rational Mechanics and Analysis*, 162(2):101–135, 2002.

[20] R. V. Kohn and G. Strang. Optimal design and relaxation of variational problems, I, II and III. *Communications on Pure and Applied Mathematics*, 39:113–137, 139–182, 353–377, 1986.

[21] B. Dacorogna. *Direct methods in the calculus of variations*. Springer-Verlag, New York, 1989.

[22] Francfort G.A., Milton G.W., and Milton G.W. Sets of conductivity and elasticity tensors stable under lamination composite-materials with Poisson ratios close to -1. *Communications on pure and applied mathematics; Journal of the mechanics and*

physics of solids, 47, 40(3, 5):257–279, 1105–1137, 1992.

[23] Clark K.E. and Milton G.W. Modeling the effective conductivity function of an arbitrary 2-dimensional polycrystal using sequential laminates. *Proceedings of the Royal Society of Edinburgh A*, 124:757–783, 1994.

[24] P. Pedregal. Laminates and microstructure. *European Journal of Applied Mathematics*, 4:121–149, 1993.

[25] M. Luskin. On the computation of crystalline microstructure. *Acta Numerica*, 5:191–257, 1996.

[26] S. Müller. Variational models for microstructure and phase transitions. In F. Bethuel et al., editors, *in: Calculus of variations and geometric evolution problems*, Springer Lecture Notes in Math. 1713, pages 85–210. Springer, Berlin, 1999.

[27] K. Bhattacharya and M. Luskin. The simply laminated microstructure in martensitic crystals that undergo a cubic-to-orthorhombic phase transformation. *Archive for Rational Mechanics and Analysis*, 149(2):123–154, 1999.

[28] G. Dolzmann. Numerical computation of rank-one convex envelopes. *SIAM Journal of Numererical Analysis*, 36(5):1621–1635, 1999.

[29] B. Li and M. Luskin. Approximation of a martensitic laminate with varying volume fractions. *Mathematical Modelling and Numerical Analysis M2AN*, 33(1):67–87, 1999.

[30] M. Ortiz and E. A. Repetto. Nonconvex energy minimization and dislocation structures in ductile single crystals. *Journal of the Mechanics and Physics of Solids*, 47(2):397–462, 1999.

[31] Ortiz M., E. A. Repetto, and L. Stainier. A theory of subgrain dislocation structures. *Journal of the Mechanics and Physics of Solids*, 48(10):2077–2114, 2000.

[32] S. Aubry, M. Fago, and M. Ortiz. A constrained sequential-lamination algorithm for the simulation of sub-grid microstructures in martensitic materials. *Computer Methods in Applied Mechanics and Engineering*, 192:2823–2843, 2003.

[33] R. V. Kohn and S. Müller. Branching of twins near an austenite-twinned-martensite interface. *Philosophical Magazine A*, 66:697–715, 1992.

[34] H. Ben Belgacem, S. Conti, A. DeSimone, and S. Müller. Energy scaling of compressed elastic films. *Archive for Rational Mechanics and Analysis*, 164:1–37, 2002.

[35] S. Conti and M. Ortiz. Dislocation microstructures and the effective behavior of single crystals. *Archive for Rational Mechanics and Analysis*, 176(1):103–147, 2005.

[36] M. Ortiz and A. Pandolfi. A class of cohesive elements for the simulation of three-dimensional crack propagation. *International Journal for Numerical Methods in Engineering*, 44:1267–1282, 1999.

[37] G. T. Camacho and M. Ortiz. Computational modelling of impact damage in brittle materials. *International Journal of Solids and Structures*, 33(20–22):2899–2938, 1996.

[38] G. Ruiz, M. Ortiz, and A. Pandolfi. Three-dimensional finite-element simulation of the dynamic brazilian tests on concrete cylinders. *International Journal for Numerical Methods in Engineering*, 48(7):963–994, 2000.

[39] G. Ruiz, A. Pandolfi, and M. Ortiz. Three-dimensional cohesive modeling of dynamic mixed-mode fracture. *International Journal for Numerical Methods in Engineering*, 52(1–2):97–120, 2001.

[40] M. Ortiz and L. Stainier. The variational formulation of viscoplastic constitutive updates. *Computer Methods in Applied Mechanics and Engineering*, 171:419–444,

1999.

[41] R.Y. Rockafellar. *Convex Analysis*. Princeton University Press, Princeton, N.J., 1970.

[42] A. Pandolfi, C. Kane, J. E. Marsden, and M. Ortiz. Time-discretized variational formulation of non- smooth frictional contact. *International Journal for Numerical Methods in Engineering*, 53(8):1801–1829, 2002.

[43] G. Friesecke and G. Dolzmann. Implicit time discretization and global existence for a quasi-linear evolution equation with nonconvex energy. *SIAM J. Math. Anal.*, 28:363–380, 1997.

[44] Radovitzky R. and Ortiz M. Error estimation and adaptive meshing in strongly nonlinear dynamic problems. *Computer Methods in Applied Mechanics and Engineering*, 172(1-4):203–240, 1999.

[45] S. Demoulini. Young measure solutions for nonlinear evolutionary systems of mixed type. *Annales de L'Institute Henri Poincaré d'Analyse Non Linéaire*, 14(1):143–162, 1997.

[46] C. R. Yu, G. Ruiz, and A. Pandolfi. Numerical investigation of the dynamic behavior of advanced ceramics. 71(4–6):897–911, 2004.

[47] F. H. Wu and L. B. Freund. Deformation trapping due to thermoplastic instability in one-dimensional wave-propagation. *Journal of the Mechanics and Physics of Solids*, 32(2):119–132, 1984.

[48] G. Dal Maso. *An introduction to* Γ*-convergence*. Birkhäuser, Boston, 1993.

[49] A. Braides and A. Defranceschi. *Homogenization of multiple integrals*. Claredon Press, Oxford, 1998.